

POLITECNICO DI TORINO

Master's Degree in
Communications and Computer Networks Engineering



Master's Degree Thesis

Study of Algorithms for GNSS-based Precise Orbit Determination in space

Supervisors

Prof. Fabio DOVIS

Dr. Alex MINETTO

Eng. Oliviero VOUCH

Eng. Simone ZOCCA

Candidate

Matteo VALVANO

Academic Year 2022/2023

Abstract

Global Navigation Satellite System (GNSS) provides accurate Positioning, Navigation and Timing (PNT) information to the users. Originally, these have been designed to serve terrestrial users, but in the last years, the interest in the use of GNSS for autonomous space navigation has significantly increased.

Over the past decades, space missions have leveraged Precise Orbit Determination (POD), which is the process of accurately estimating and tracking both the position and velocity of spacecraft along the orbit. This method usually relies on post-processing computation, based on range and Doppler tracking services offered by federated networks, such as NASA Deep Space Network (DSN), managed by the ground segment. On the contrary, exploiting real-time, in-orbit GNSS-based navigation systems would make the spacecraft more autonomous, reducing the costs and the effort of ground operations. The use of in-orbit GNSS receivers has been validated in low orbits, as in Low Earth Orbits (LEOs), up to a distance of approximately 150.000 km from the Earth's surface. The use of GNSS in space applications is hence becoming attractive even for spacecraft navigation at larger distances, for example, in lunar missions. However, deploying GNSS receivers to lunar distances is a challenging task due to multiple factors. First of all, the received signals are characterized by low power levels, especially at altitudes above the GNSS constellation. In these conditions, the signals transmitted by the main antenna lobes suffer occultation effects, being received from satellites orbiting on the opposite side of the Earth. Side lobes, on the other hand, only provide low-power signals in the spacecraft direction. Besides, signal availability is drastically impaired by poor geometry, leading to accuracy degradation in the positioning and navigation solutions. Additionally, GNSS space-born receivers could experience high relative dynamics with respect to the GNSS satellites, which are responsible for both Doppler frequency and Doppler rate.

This thesis work aims at studying and implementing techniques to increase the positioning accuracy and independence of GNSS space-born receivers, to get the best from a harsh scenario like that of space missions. The targeted strategy involves

the extension of pre-existent algorithms, like the Extended Kalman Filter (EKF), introducing external aidings allowing the enhancement of the position estimation process. In particular, the aiding consists of the expected orbital trajectory that a spacecraft is planned to follow and it would allow excellent performances the more the matching between the last estimated position and its ideal correspondent point onto the aiding trajectory is accurate. However, such matchings are not so trivial and should be the subject of further studies. In light of this, approximate matchings have been used to provide quite good performances.

The performance of the proposed methodology called the Trajectory-Aware Extended Kalman Filter (TA-EKF), is investigated through a dedicated framework that simulates Earth-Moon Transfer Orbit (MTO) mission scenarios and associated GNSS measurements. Monte Carlo analyses are utilized to statistically assess the proposed solution against a standalone EKF architecture.

Table of Contents

List of Tables	VIII
List of Figures	IX
Acronyms	XII
1 Introduction	1
1.1 GNSS fundamentals	2
1.1.1 The PVT problem	4
1.2 Space exploration	10
1.2.1 Critical issues of using GNSS in space	12
1.3 Purpose and Development of the work	13
2 PVT Filters	15
2.1 Least Mean Square Filter	15
2.1.1 LMS Position estimation	17
2.1.2 LMS Velocity estimation	18
2.1.3 LMS Estimation error	19
2.2 Kalman Filter	20
2.2.1 Linearized Kalman filter	22
2.2.2 Extended Kalman Filter	25
2.2.3 Dynamic model for position states	27
2.2.4 Trajectory-Aware Extended Kalman Filter	29
2.2.5 Implementing Kalman Filtering for GNSS Applications	30
2.2.6 Trajectory-Aware EKF validation testing	32
2.2.7 Choosing the aiding	34
2.3 Comments on navigation filters	34
3 Simulation framework	37
3.1 Environment background	37

3.2	Receiver	39
3.2.1	Receiver antenna pattern	39
3.2.2	Receiver clock model	40
3.2.3	Receiver trajectory	42
3.3	GNSS Satellites	43
3.3.1	GPS constellation	44
3.3.2	Galileo constellation	46
3.3.3	Geometric and Radiometric visibility	47
3.4	Observables generation	50
3.4.1	Measurement noise	52
3.5	Navigation filters	53
4	Simulation results	57
4.1	Mission overview	57
4.1.1	GNSS satellite distribution	60
4.1.2	Expected GNSS performances	62
4.2	Case study: LuGRE planned mission period	64
4.2.1	Navigation filters comparison	68
5	Conclusions	75
	Bibliography	79

List of Tables

2.1	Positioning error (m) for plain EKF and TA-EKF considering 2000 epochs at 10 Hz.	34
3.1	Hadamard variance parameters.	41
3.2	Satellite antenna body-fixed coordinate system.	44
3.3	Data associated with the GPS-constellation list generated by the framework.	46
3.4	Link budget parameters.	49
3.5	1- σ noise model parameters.	52
4.1	Positioning error for plain EKF and TA-EKF considering 7200 epochs at 1 Hz.	69

List of Figures

1.1	LuGRE concept of operations.	2
1.2	GNSS Trilateration: where all spheres intersect correspond to the user GNSS time and position.	5
1.3	The Global Exploration Roadmap.	12
2.1	KF block diagram.	23
2.2	Nominal and actual trajectories for a Linearized KF.	24
2.3	Estimated and actual trajectories for a Linearized KF.	25
2.4	PV model.	27
2.5	Samarcanda dataset. Comparison between the ground-truth trajectory and the estimated one.	32
2.6	Empirical Cumulative Distribution Function (ECDF) for the positioning error in ECEF-coordinates and Positioning error at 25-th, 50-th, 75-th and 95-th percentiles. Comparison between plain EKF and TA-EKF filters.	33
	(a)	33
	(b)	33
3.1	ECEF reference frame and Earth representation.	38
3.2	LuGRE receiver antenna pattern 2D (a) and 3D (b) representation. Constant for every azimuthal angle.	39
	(a)	39
	(b)	39
3.3	Hadamard deviation plots of three sample oscillators reported in Table 3.1.	41
3.4	Trajectory overview according to the ECEF reference frame with a temporal resolution of 15 minutes between subsequent points.	42
3.5	Station vehicle IGS reference system with sun and probe (receiver) steering vectors.	43
3.6	GPS IIR model antenna pattern 2D (a) and 3D (b) representation. Azimuthal angle cuts every 10 degrees.	45

(a)	45
(b)	45
3.7 GPS IIR-M model antenna pattern 2D (a) and 3D (b) representation. Azimuthal angle cuts every 10 degrees.	45
(a)	45
(b)	45
3.8 GPS IIF model antenna pattern 2D (a) and 3D (b) representation. Azimuthal angle cuts every 10 degrees.	45
(a)	45
(b)	45
3.9 Galileo ESA/ESOC model antenna pattern 2D (a) and 3D (b) representation. Constant for every azimuthal angle.	47
(a)	47
(b)	47
3.10 SV geometric visibility example with Earth occultation angles and distances.	48
3.11 Simulation framework example. Satellites showing their antenna patterns are RF-visible.	50
3.12 1- σ noise model for Pseudorange (a) and Doppler shift (b) measurement noise.	53
(a)	53
(b)	53
4.1 Mission Orbit Radius (a) and Velocity (b) as function of elapsed time.	58
(a)	58
(b)	58
4.2 NASA's Wilkinson Microwave Anisotropy Probe (WMAP) phasing loops. WMAP orbits around Earth waiting for the moon to move into the right position. This is about a three week process.	59
4.3 Doppler shift (a) and Doppler rate (b) for GPS station vehicle SVN56 as function of the mission elapsed time.	59
(a)	59
(b)	59
4.4 Radiometric visibility ($C/N_0 \geq 20$ dB - Hz) as function of mission distance (a) and elapsed time (b).	60
(a)	60
(b)	60
4.5 Radiometric visibility ($C/N_0 \geq 23$ dB - Hz) as function of mission distance (a) and elapsed time (b).	61
(a)	61
(b)	61

4.6	Least Square GDOP and reciprocal condition of Gramian matrix as function of mission distance (a) and elapsed time (b).	62
	(a)	62
	(b)	62
4.7	Error covariance ellipsoids from EKF results and covariance anomalies due to bad geometry.	63
4.8	GDOP (a), Satellite Visibility (b) and Receiver Dynamics (c) at covariance ellipsoid epochs.	64
	(a)	64
	(b)	64
	(c)	64
4.9	LuGRE Operations Schedule During Transit.	65
4.10	Mission point 2: Orbit Radius (a) and Velocity (b) as function of mission elapsed time.	65
	(a)	65
	(b)	65
4.11	Mission segment analyzed velocity states.	66
4.12	Mission segment framework realization.	66
4.13	Mission segment satellite Radiometric visibility ($C/N_0 \geq 23$ dB – Hz) as function of mission distance (a) and elapsed time (b).	67
	(a)	67
	(b)	67
4.14	Least Square GDOP and reciprocal condition of Gramian matrix as function of the mission segment distance (a) and elapsed time (b).	67
	(a)	67
	(b)	67
4.15	Doppler shift (a) and Doppler rate (b) for GPS station vehicle SVN56 as function of the mission segment elapsed time. Note that the station vehicle SVN56 gets out of radiometric visibility after 4490 seconds since the mission segment started.	68
	(a)	68
	(b)	68
4.16	ECDF for the positioning error in ECEF-coordinates for LMS, plain EKF and TA-EKF filters (a) and cumulative error comparison for EKF and TA-EKF (b).	69
	(a)	69
	(b)	69
4.17	Time-series of the 1σ -dispersion of the navigation filter estimates for the Position (a), Velocity (b), Clock Bias (c) and Clock Drift (d) states. Comparison between plain EKF and TA-EKF.	70
	(a)	70

(b)	70
(c)	70
(d)	70
4.18 Mission point error covariance ellipsoids overview.	71
4.19 Time series of the positioning error of 100 Monte Carlo realizations.	
Comparison between plain EKF (a) and TA-EKF (b).	71
(a)	71
(b)	71
4.20 Convergence of standard deviation of state estimation uncertainty	
from KF compared to GDOP.	72
(a)	72
(b)	72
(c)	72
(d)	72
4.20 Convergence of standard deviation of state estimation uncertainty	
from KF compared to GDOP.	73
(e)	73
(f)	73
(g)	73
(h)	73

Acronyms

ASI Agenzia Spaziale Italiana

BDS BeiDou Navigation Satellite System

BCE Broadcast Ephemeris

BDS BeiDou

BF Body-Fixed

C/N_0 Carrier-to-Noise power density ratio

CNR Carrier-to-Noise power density ratio

CNSA China National Space Administration

DoD Department of Defence

DSN Deep Space Network

DTE Direct To Earth

ECDF Empirical Cumulative Distribution Function

ECEF Earth-Centered Earth-Fixed

ECI Earth-Centered Inertial

ECM Error Covariance Matrix

EGNOS European Geostationary Navigation Overlay System

EIRP Effective Isotropic Radiated Power

EKF Extended Kalman Filter

ESA European Space Agency
ESOC European Space Operations Center
FOC Full Operational Capability
RF Radio-Frequency
GCF Gain Correction Factor
GEO Geostationary Orbit
GDOP Geometric Dilution Of Precision
GLONASS Globalnaya Navigazionnaya Sputnikovaya Sistema
GNSS Global Navigation Satellite System
GPS Global Positioning System
HEO Highly Elliptical Orbit
IGS International GNSS Service
IOV In Orbit Validation
ISS Information Satellite System
JAXA Japan Aerospace Exploration Agency
KF Kalman Filter
LEO Low Earth Orbit
LLSME Linear Least Mean Squares Estimator
LQE Linear Quadratic Estimator
LOS Line-Of-Sight
LMS Least-Mean-Squares
LMSE Least-Mean-Squares Estimator
LuGRE Lunar GNSS Receiver Experiment

MMS USO Magnetospheric MultiScale Ultra Stable Oscillator

MTO Earth-Moon Transfer Orbit

NASA National Aeronautics and Space Administration

NavIC Navigation with Indian Constellation (Indian Regional Navigation Satellite System)

ODTS Orbit Determination and Time Synchronization

OF Orbital Filter

PNT Positioning, Navigation and Timing

POD Precise Orbit Determination

PV Position-Velocity

PVT Position, Velocity and Timing

RAFS Rubidium Atomic Frequency Standard

RE Radius Earth

SBAS Satellite-Based Augmentation System

SV Station Vehicle

TA-EKF Trajectory-Aware Extended Kalman Filter

TSV Terrestrial Service Volume

UERE User Equivalent Range Error

UTC Universal Time Coordinated

VCTCXO Voltage Controlled Temperature Compensated Crystal Oscillator

WGN White Gaussian Noise

WLMS Weighted Least Mean Square

WMAP Wilkinson Microwave Anisotropy Probe

Chapter 1

Introduction

The following work was inspired by the Lunar GNSS Receiver Experiment (LuGRE) project [1]. LuGRE is an upcoming mission that is a joint NASA-Italian Space Agency flight demonstration payload. The mission consists of several experiments that will be conducted on the moon. It will launch at the end of 2023 using a Space X Falcon 9 rocket, and the LuGRE receiver and antenna will be incorporated into the Firefly Blue Ghost 1 lander (Fig. 1.1).

The main goal of LuGRE is to extend GNSS-based navigation to the moon by setting up a receiver on the moon and analyzing GNSS signals. The mission will also collect GNSS data in transit and use it to develop GNSS receivers tailored for use on the moon. The payload consists of a high-gain L-band antenna, a low-noise amplifier, and a weak-signal GNSS receiver. The receiver will receive and track GPS L1 C/A and L5 signals, Galileo E1 and E5a signals, and produce pseudorange, carrier phase, and Doppler measurements. The receiver also has the capacity to record raw L1 and L5 I/Q baseband samples. LuGRE will perform its operations on the lunar surface and during transit between Earth and the moon. The Science Team has identified 10 science investigations and more than a dozen additional efforts. The preliminary examination of the LuGRE operations shows high signal visibility throughout the mission and the ability to acquire signals in post-processing.

This thesis aims to analyze space applications of GNSS, evaluate its critical issues and provide some tools to try to overcome them by reconstructing an environment able to simulate GNSS measures to be processed through different navigation filters.

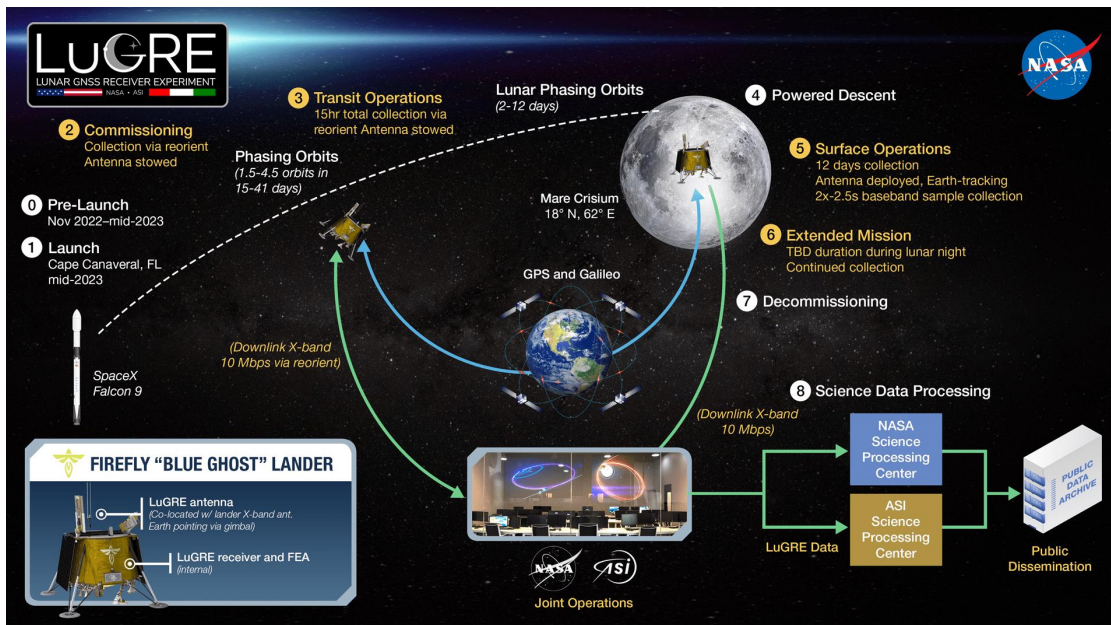


Figure 1.1: LuGRE concept of operations.

1.1 GNSS fundamentals

Global Navigation Satellite System (GNSS) refers to a constellation of satellites providing signals from space that transmit positioning and timing data to GNSS receivers, providing, by definition, global coverage. The receivers then use this data to determine location.

The performance of GNSS is assessed using four criteria:

- **Accuracy:** the difference between a receiver's measured and real position, speed or time.
- **Integrity:** a system's capacity to provide a threshold of confidence and, in case of an anomaly in the positioning data, an alarm.
- **Continuity:** a system's ability to function without interruption.
- **Availability:** the percentage of time a signal fulfils the above accuracy, integrity and continuity criteria.

In general, this performance can be improved by regional Satellite-Based Augmentation Systems (SBASs), such as the European Geostationary Navigation Overlay

System (EGNOS), which improves the accuracy and reliability of GPS information by correcting signal measurement errors by providing information about the integrity of its signals.

A Global Navigation Satellite System is composed of three major components or “segments”:

- **Space segment:** it consists of a constellation of satellites appropriately arranged to broadcast satellite positioning, timing, and navigation data from space to GNSS receivers, and provide the desired coverage.
- **Control segment:** it is a network composed of monitor stations constantly checking the signal and status of the satellites, master control stations which analyse the signals and transmit orbit and time corrections to the satellites through data uploading stations, to adjust the satellites’ orbit parameters and onboard high-precision clocks when necessary to maintain accuracy.
- **User segment:** consists of the user equipment allowing to perform signal reception to determine user position, velocity and time.

There are several GNSSs in operation today, including:

- **GPS:** the United States Global Positioning System.

GPS is the pioneer in the world of GNSS been operative since 1978 and made available for global use in 1994.

The invention of GPS was driven by the requirement for a standalone navigation system for military purposes, with the United States Department of Defence (DoD) being the first to recognize this need. The system was designed with a high level of complexity to ensure high accuracy and protect against jamming and counterfeiting attempts. Eventually, GPS became available to the public.

GPS operates in a frequency band referred to as the L-Band, a portion of the radio spectrum between 1 and 2 GHz. L-Band was chosen for several reasons, including:

- Ionospheric delay is more significant at lower frequencies
- Simplification of antenna design
- Minimize the effect that weather has on GPS signal propagation

Currently, with its 31 operative satellites, GPS is considered the most precise navigation system globally. The newest iteration of GPS satellites utilizes highly accurate rubidium clocks, which are further synchronized by even more precise Caesium clocks based on the ground.

- **GLONASS** (Globalnaya Navigazionnaya Sputnikovaya Sistema), Russia’s Global Navigation Satellite System, which is Russia’s version of GPS. Its development began in 1976 with the Soviet Union. Mainly designed for Russian areas, when used alone, GLONASS doesn’t provide as strong of coverage compared to GPS. As of December 2022, 144 GLONASS navigation satellites have been launched, of which 132 reached the correct orbit and 23 are currently operational.
- **Galileo**, the European Union’s GNSS. It is Europe’s GNSS system that’s compatible with GPS and GLONASS. It started providing service in December 2016. As of August 2022, 28 Galileo satellites have been launched, of which 4 In Orbit Validation (IOV) and 24 Full Operational Capability (FOC). The 2 GIOVE prototype vehicles were retired in 2012, 24 satellites are operational, 1 is not available and 3 are currently not usable.
- **BeiDou**, China’s Navigation Satellite System (BDS). As of January 2022, 44 satellites are operational
- **NavIC**, India’s Navigation Satellite System with Indian Constellation, whose constellation consists of 7 satellites.

In addition to these five major GNSS, there are also regional and smaller-scale systems in operation around the world.

1.1.1 The PVT problem

In principle, GNSS receivers work based on a technique known as *Trilateration*, based on measuring distances.

Each satellite broadcasts a signal for the GNSS receiver to pick up at a specific time and distance, which defines a sphere around the satellite. Where all spheres “detected” by the receiver intersect determines the position of the user, as depicted in Figure 1.2.

In general, the positioning problem is stated as a PVT problem, which is one of the most important issues of satellite-based navigation systems. PVT is an acronym that stands for Position (Latitude, Longitude, Height), Velocity (North, East, Up) and precise Time in Universal Time Coordinated (UTC).

GNSS receivers determine the user position, velocity, and precise time by processing the signals broadcasted by satellites. Since the satellites are always in motion, the receiver has to continuously acquire and track the signals from the satellites in view, to compute an uninterrupted solution, as desired in most applications.

Any navigation solution provided by a GNSS receiver is based on the computation of its distance to a set of satellites: it consists in measuring the propagation time

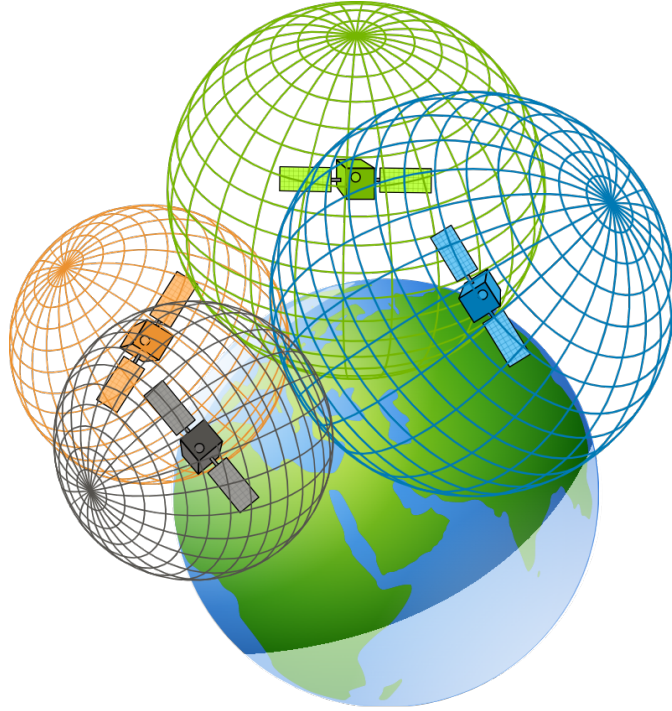


Figure 1.2: GNSS Trilateration: where all spheres intersect correspond to the user GNSS time and position.

it takes for an incoming signal transmitted by a satellite at a known location to reach a user receiver at the speed of light, according to local clocks of satellite and receiver. Multiplying this time interval by the speed of light in the vacuum, the time difference is transformed into a very rough estimate of the emitter-to-receiver distance, called Pseudorange. This corresponds to the *pseudo*-distance from the receiver antenna to the satellite antenna, including receiver and satellite clock offsets and other biases, such as atmospheric delays.

For a signal from the satellite (s) the pseudorange $P_r^{(s)}$ can be expressed by using the signal reception time $t_{rx}^{(s)}|_r$ measured by the receiver clock and the signal transmission time $t_{tx}^{(s)}|_s$ measured by the satellite clock as:

$$P_r^{(s)} = c(t_{rx}^{(s)}|_r - t_{tx}^{(s)}|_s) \quad (1.1)$$

where:

$$t_{rx}^{(s)}|_r = t_{rx}^{(s)} + \Delta t_r \quad (1.2)$$

$$t_{tx}^{(s)}|_s = t_{tx}^{(s)} + \Delta t_s \quad (1.3)$$

More specifically, not only does the pseudorange equation have to consider the geometric range $\rho_r^{(s)}$ between satellite and receiver antennas, namely their mutual geometric distance, but it has also to take into account the receiver and satellite clock biases Δt_r and Δt_s with respect to the common UTC reference time, the ionospheric and tropospheric delays $I_r^{(s)}$ and $T_r^{(s)}$ and the measurement error ϵ_P .

$$\begin{aligned}
 P_r^{(s)} &= c[(t_{rx}^{(s)} + \Delta t_r) - (t_{tx}^{(s)} + \Delta t_s)] + I_r^{(s)} + T_r^{(s)} + \epsilon_P \\
 &= c(t_{rx}^{(s)} - t_{tx}^{(s)}) + c(\Delta t_r - \Delta t_s) + I_r^{(s)} + T_r^{(s)} + \epsilon_P \\
 &= \rho_r^{(s)} + c(\Delta t_r - \Delta t_s) + I_r^{(s)} + T_r^{(s)} + \epsilon_P
 \end{aligned} \tag{1.4}$$

In light of this, many complications arise. The major one is that the receiver is using its clock to tag the received time, often supplied by a very inexpensive crystal oscillator. The speed of light is about $3 \cdot 10^8$ meters per second, thus very small errors in the receiver clock can cause large range errors. This is solved by including the time bias of the receiver clock in the set of unknowns.

Hence, there are four unknowns at each time step where a solution is computed: three for position and one for time. As a consequence, the minimum number of satellites in view needed for the determination of a solution is four. In addition, as a result of this formulation, the receiver is able to consistently provide precise time information. Specifically, the receiver generates a new estimate of GPS time at each interval, typically occurring once per second.

As mentioned before, the location of the satellites is needed to determine the PVT. The signal that allows the determination of the precise location, velocity, and clock state of a satellite is conveyed through the message data. The message data provides a sequence of parameters that are utilized in an orbit model, allowing for accurate calculations of the satellite's position, speed, and time.

In particular, the information is divided into two pieces: the Broadcast Ephemeris (BCE) and the Almanac.

The BCE provides information on the satellite position and velocity, which is very accurate and stays that way for a day or so. The information about the bias of the satellites' onboard clock is provided too, but, since the atomic clock of the satellites wanders a few nanoseconds per day, the inaccuracy in the clock parameters in the BCE is a major error source. It takes a maximum of 3 minutes of tracking to get the ephemeris from a satellite, so this data repeats every 3 minutes, and they cannot be used for generating a solution until the BCE is completely received.

The Almanac is a lower accuracy set of parameters provided for all the satellites in orbit, to help receivers plan satellite tracking and acquire satellite signals. This data cycles more slowly and takes 12.5 minutes to repeat. Usually, all satellites broadcast the same almanac and, among others, there are also the values needed to convert the GPS Time used by the satellites to UTC.

The user, by measuring four pseudoranges with respect to four satellites with known coordinates, can determine four unknowns:

- (x_u, y_u, z_u) User coordinates
- δt_u Bias of the user receiver clock w.r.t. the GNSS time scale.

These unknowns can be obtained through a system of four pseudorange equations.

$$\begin{cases} \rho_1 = \sqrt{(x_1 - x_u)^2 + (y_1 - y_u)^2 + (z_1 - z_u)^2} + b_{ut} \\ \rho_2 = \sqrt{(x_2 - x_u)^2 + (y_2 - y_u)^2 + (z_2 - z_u)^2} + b_{ut} \\ \rho_3 = \sqrt{(x_3 - x_u)^2 + (y_3 - y_u)^2 + (z_3 - z_u)^2} + b_{ut} \\ \rho_4 = \sqrt{(x_4 - x_u)^2 + (y_4 - y_u)^2 + (z_4 - z_u)^2} + b_{ut} \end{cases} \quad (1.5)$$

where

- ρ_j : j -th measured pseudorange (pseudo-sphere radius)
- (x_j, y_j, z_j) : known j -th satellite coordinates (centre of pseudo-sphere)
- $b_{ut} = c \cdot \delta t_u$: range bias in meters due to misalignment of user timescales (unknown).

The solution of non-linear equations can be simplified considering the large distance of the satellites with respect to the users. This would allow for reduced computational complexity.

The equation of the pseudo-sphere can be linearized, thus transforming the trilateration process in the intersection of the planes tangent to the pseudo-sphere in the user position. The process of linearization consists in considering the Taylor expansion of the multidimensional equation truncated at the first order.

Hence, given a user state guess $(\hat{x}_u, \hat{y}_u, \hat{z}_u, \hat{b}_{ut})$ and computed the associated approximate pseudorange as:

$$\hat{\rho}_j = \sqrt{(x_j - \hat{x}_u)^2 + (y_j - \hat{y}_u)^2 + (z_j - \hat{z}_u)^2} + \hat{b}_{ut} \quad (1.6)$$

The linearized equation is given by:

$$\begin{aligned}
 \rho_j &= \hat{\rho}_j + \dots \\
 &+ \left. \frac{\partial \rho_j}{\partial x_u} \right|_{x_u = \hat{x}_u} (x_u - \hat{x}_u) + \dots \\
 &+ \left. \frac{\partial \rho_j}{\partial y_u} \right|_{y_u = \hat{y}_u} (y_u - \hat{y}_u) + \dots \\
 &+ \left. \frac{\partial \rho_j}{\partial z_u} \right|_{z_u = \hat{z}_u} (z_u - \hat{z}_u) + \dots \\
 &+ \left. \frac{\partial \rho_j}{\partial b_{ut}} \right|_{b_{ut} = \hat{b}_{ut}} (b_{ut} - \hat{b}_{ut})
 \end{aligned} \tag{1.7}$$

By rewriting the linearized equation, it can be expressed as a function of the displacement with respect to the approximation point:

$$\Delta \rho_j = a_{x_j} \Delta x_u + a_{y_j} \Delta y_u + a_{z_j} \Delta z_u - \Delta b_{ut} \tag{1.8}$$

where:

$$\Delta \rho_j = \hat{\rho}_j - \rho_j$$

$$\Delta x_u = x_u - \hat{x}_u$$

$$\Delta y_u = y_u - \hat{y}_u$$

$$\Delta z_u = z_u - \hat{z}_u$$

$$\Delta b_{ut} = b_{ut} - \hat{b}_{ut}$$

$$a_{x_j} = \frac{x_j - \hat{x}_u}{\hat{r}_j}$$

$$a_{y_j} = \frac{y_j - \hat{y}_u}{\hat{r}_j}$$

$$a_{z_j} = \frac{z_j - \hat{z}_u}{\hat{r}_j}$$

$\hat{r}_j = \sqrt{(x_j - \hat{x}_u)^2 + (y_j - \hat{y}_u)^2 + (z_j - \hat{z}_u)^2}$ (geometrical distance between the linearization point and the j -th satellite)

The linearized navigation solution can be derived from the linearized model:

$$\begin{cases}
 \Delta \rho_1 = a_{x_1} \Delta x_u + a_{y_1} \Delta y_u + a_{z_1} \Delta z_u - \Delta b_{ut} \\
 \Delta \rho_2 = a_{x_2} \Delta x_u + a_{y_2} \Delta y_u + a_{z_2} \Delta z_u - \Delta b_{ut} \\
 \Delta \rho_3 = a_{x_3} \Delta x_u + a_{y_3} \Delta y_u + a_{z_3} \Delta z_u - \Delta b_{ut} \\
 \Delta \rho_4 = a_{x_4} \Delta x_u + a_{y_4} \Delta y_u + a_{z_4} \Delta z_u - \Delta b_{ut}
 \end{cases} \tag{1.9}$$

In matricial form:

$$\Delta \boldsymbol{\rho} = \mathbf{H} \Delta \mathbf{x} \quad (1.10)$$

$$\Delta \boldsymbol{\rho} = \begin{bmatrix} \Delta \rho_1 \\ \Delta \rho_2 \\ \Delta \rho_3 \\ \Delta \rho_4 \end{bmatrix} \quad (1.11)$$

$$\mathbf{H} = \begin{bmatrix} a_{x_1} & a_{y_1} & a_{z_1} & 1 \\ a_{x_2} & a_{y_2} & a_{z_2} & 1 \\ a_{x_3} & a_{y_3} & a_{z_3} & 1 \\ a_{x_4} & a_{y_4} & a_{z_4} & 1 \end{bmatrix} \quad (1.12)$$

$$\Delta \mathbf{x} = \begin{bmatrix} \Delta x_u \\ \Delta y_u \\ \Delta z_u \\ -\Delta b_{ut} \end{bmatrix} \quad (1.13)$$

In the case of four satellites, the navigation solution is calculated as:

$$\Delta \mathbf{x} = \mathbf{H}^{-1} \Delta \boldsymbol{\rho} \quad (1.14)$$

provided that the geometric matrix of the positioning problem \mathbf{H} is non-singular, namely, invertible.

In general, a larger number of satellites is available, therefore a least square solution must be used.

$$\Delta \mathbf{x} = (\mathbf{H}^T \mathbf{H})^{-1} \mathbf{H}^T \Delta \boldsymbol{\rho} \quad (1.15)$$

As for the positioning errors, they propagate according to the same model, namely:

$$\Delta \boldsymbol{\rho} + \boldsymbol{\delta} \boldsymbol{\rho} = \mathbf{H}(\Delta \mathbf{x} + \boldsymbol{\delta} \mathbf{x}) \quad (1.16)$$

from which it can be derived:

$$\boldsymbol{\delta} \mathbf{x} = (\mathbf{H}^T \mathbf{H})^{-1} \mathbf{H}^T \boldsymbol{\delta} \boldsymbol{\rho} \quad (1.17)$$

Equation (1.17) explains the positioning error dependence on the satellite geometry and the error in pseudorange estimation.

Considering the covariance matrix of the position error $\boldsymbol{\delta} \mathbf{x}$, the elements on the diagonal are the variance of the error in the different dimensions (including time), whereas the off-diagonal terms indicate the level of cross-correlation between the variables.

In particular, it can be derived:

$$cov(\delta \mathbf{x}) = \mathbf{G} \cdot \sigma_{URE}^2 \quad (1.18)$$

where:

- $\mathbf{G} = (\mathbf{H}^T \mathbf{H})^{-1} = [g_{ij}]$ is the *Geometric Factor*, such that:

$$\begin{aligned} \sigma_{x_u}^2 &= g_{11} \cdot \sigma_{URE}^2 \\ \sigma_{y_u}^2 &= g_{22} \cdot \sigma_{URE}^2 \\ \sigma_{z_u}^2 &= g_{33} \cdot \sigma_{URE}^2 \\ \sigma_{b_{ut}}^2 &= g_{44} \cdot \sigma_{URE}^2 \end{aligned} \quad (1.19)$$

- σ_{URE}^2 is the variance associated with the pseudorange measurement error

The standard deviation of the positioning error can be obtained as:

$$\sigma_{\mathbf{x}} = \sqrt{\sigma_{x_u}^2 + \sigma_{y_u}^2 + \sigma_{z_u}^2 + \sigma_{b_{ut}}^2} = GDOP \cdot \sigma_{URE} \quad (1.20)$$

where the Geometric Dilution Of Precision (GDOP) is defined as:

$$GDOP = \sqrt{g_{11} + g_{22} + g_{33} + g_{44}} = \sqrt{tr(\mathbf{G})} \quad (1.21)$$

1.2 Space exploration

In recent days, several space agencies are renewing their interest in Lunar exploration, which involves both the public and private sectors, and will offer new opportunities for a multitude of disciplines from planetary geology to astronomy and astrobiology. Of course, this renewing interest aim at the human return to the Moon, with the goal, among the others, of the creation of lunar bases toward deep space expeditions like Mars (Fig. 1.3).

This growing trend in the number of missions to the Moon is creating demand for various research on a system which could increase the robustness of navigation architectures and improve their autonomous operation capabilities. In the past, lunar expeditions have almost entirely relied on measurements from Earth and infrastructures used in terrestrial missions. The benefits of these relay infrastructures were also demonstrated by the recent far-side lunar mission, like for example the landing of the Chinese Chang'E 4 mission (focused on relaying telemetry to the ground rather than providing an independent orbit determination and navigation solution). Moreover, GNSSs are currently used in space missions, not only in terms of navigation sensors but also as science instruments. Although their use has been generally limited to orbits below the GNSS constellations, recent studies have

shown that GNSS-based navigation for Geostationary Orbit (GEO) and Highly Elliptical Orbit (HEO) missions is feasible and with relatively good performances, demonstrating its applicability to a wide range of space missions. Therefore, these studies show that GNSS signals from Earth can be received at the Moon's altitude, effectively providing support for orbit determination and landing operations on the near side. However, the Earth-based techniques currently adopted for navigation with satellites in cislunar space are not able to cover all the needs for future exploration, both in terms of service performance (i.e., need to land within 100 m of a predetermined location on the lunar surface) and accessibility. These technologies alone do not support far-side operations (the South Pole and the far side are not always accessible by Earth-based ground stations) and will not reach the accuracy required by the Global Exploration Roadmap Critical Technology Needs.

These problems are caused by the critical conditions of the lunar environment, where the coverage is limited and the signals are weaker. Furthermore, for future missions, precise data concerning the position of rovers on the Moon's surface will become of vital importance, and an autonomous navigation system capable of real-time absolute positioning on the Moon will be crucial for the future of lunar exploration. The topic has been widely discussed in the literature since the 1970s when Farquhar described how satellites in Earth-Moon libration points could be used to support satellite navigation in cislunar space. Other works have gone further in this argument, assessing different lunar navigation infrastructures based on Earth-Moon Lagrange point orbiters providing one-way Doppler measurements together with Earth GPS signals showing results better than 1 km for positioning and 5 cm/s for velocity in cislunar space. For all these reasons, several space agencies have proposed dedicated systems to address these problems and provide navigation services for future lunar missions. The Russian satellite maker, Information Satellite System (ISS) JSC, proposed a concept that envisions the deployment of a full constellation of 24 satellites around the Moon between 2036 and 2040; in the US, Lockheed Martin has proposed Parsec; Japan Aerospace Exploration Agency (JAXA) has recently launched a study which will consider possible lunar positioning satellite systems; China recently announced that its space agency China National Space Administration (CNSA) is planning to set up a satellite constellation around the Moon to provide navigation services. On top of these initiatives, NASA has proposed the LunaNet framework to enable interoperability among different lunar navigation service providers. In this context, the European Space Agency (ESA) has proposed a concept called Moonlight that aims to provide navigation services to institutional and commercial lunar missions. The ESA's vision represented by the Moonlight initiative is to foster the creation and development of dedicated lunar navigation services, to be delivered by private partners. These services will support the next generation of institutional and private lunar exploration missions, including enhancing the performance of those missions currently under definition

and creating new possibilities.

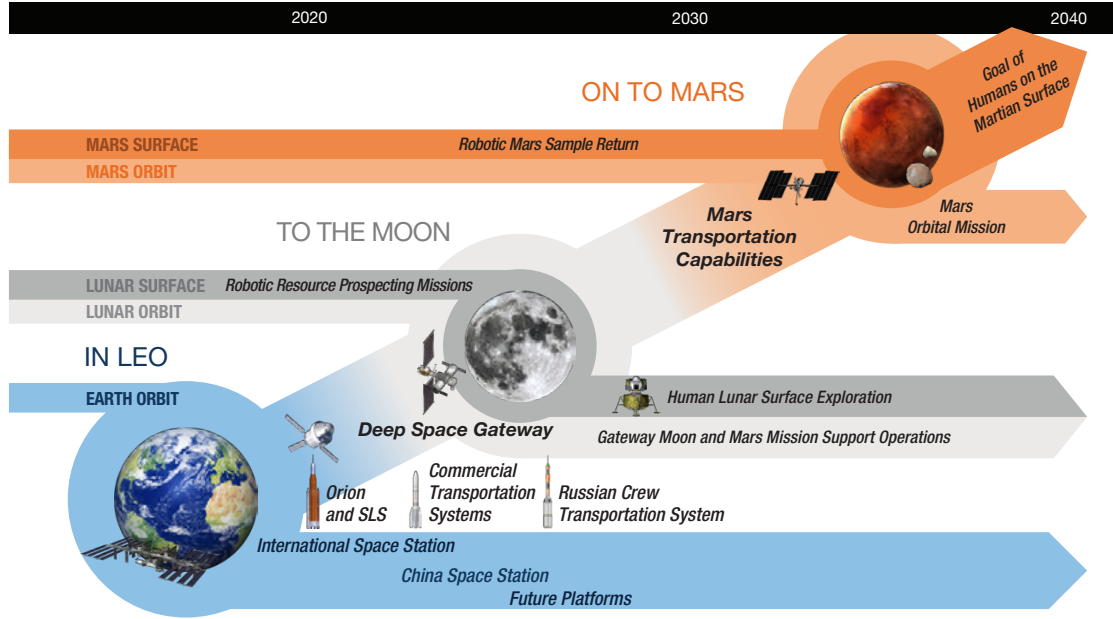


Figure 1.3: The Global Exploration Roadmap.

1.2.1 Critical issues of using GNSS in space

Nowadays' GNSS constellations were designed to provide very qualitative performances on Earth. However, their geometry is not as good when coming to space applications.

The quality of GNSS positioning, strongly relates to how the satellites used for solving the PVT are spread around the user receiver. The better their distribution, the better the positioning accuracy. The geometric dependency of the positioning precision is expressed by the Equation (1.20). The term σ_{UERE} takes into account all error contributions of the system such as propagation errors and ephemeris errors, but in the condition in which all the biases were previously compensated. Going into detail, UERE stands for user equivalent range errors and its standard deviation is computed, as anticipated before, as the root mean square error of the ranging errors affecting the user position. It is strongly related to the received signal power as well, which depends on the distance between transmitter and receiver antennas, which can not be overlooked in this context.

External aidings are fundamental to face the harsh space environment characterized by intrinsic poor geometry and reduced visibility. Furthermore, the relative

dynamics between the receiver and the transmitters are considerably higher than the routine values for terrestrial applications. As a consequence, the GNSS space signals suffer from larger values of Doppler shifts and Doppler rates make the traditional GNSS receivers unable to correctly perform the acquisition and the tracking stage. Summing up, assistance information regarding these values must be provided to the GNSS receiver through a more advanced architecture. An example of this is the use of an adaptive Orbital Filter (OF) to aid the acquisition and tracking of very weak signals leading to higher accuracy in the navigation solutions.

1.3 Purpose and Development of the work

Although GNSSs were originally designed for terrestrial users, the space sector has increasingly adopted GNSS-based navigation systems. Recent advancements in space-borne receivers have allowed for the expansion of space Positioning, Navigation and Timing (PNT) applications. However, current Orbit Determination and Time Synchronization (ODTS) algorithms rely on Direct To Earth (DTE) ranging capabilities and long-term post-processing solutions, which may not be sufficient for deep-space exploration. To address this, a customized Extended Kalman Filter (EKF) architecture called the Trajectory-Aware Extended Kalman Filter (TA-EKF) has been proposed as OF for GNSS-based navigation to the Moon. This solution integrates information about the planned mission trajectory to correct the EKF state-prediction and improve positioning accuracy in the Earth-Moon Transfer Orbit (MTO) environment. Monte Carlo analyses were used to test the TA-EKF against a plain EKF architecture. Moreover, it was built a framework able to simulate a GNSS environment within which test different PVT filters to compare their performances in space applications.

Chapter 2 presents the principle of working of the three navigation filters for PVT estimation that will be collated (*LMS*, *EKF* and *TA-EKF*).

In Chapter 3, the simulation framework is presented with all assumption made to keep the system as simple as qualitatively valid.

Chapter 4 shows the results obtained from experimenting the PVT filters within the simulation framework, discussing them and proving the framework qualitative reliability.

Finally, in Chapter 5, the conclusions drawn from this work are reported.

Chapter 2

PVT Filters

This chapter provides a discussion of some classic and innovative signal-processing techniques that address positioning and navigation problems. All these methods are based on the Bayesian estimation theory. Bayesian models allow the inclusion of prior knowledge about the phenomenon being modelled, handle sequential arrival of data, and provide online inference.

Despite being Bayesian estimators, they are usually referred to as “filters”. Historically, a filter referred to a physical device used to separate unwanted components from liquid-solid mixtures. Later, the term was applied to analogue circuits that filtered electronic signals by selectively reducing unwanted frequencies. In the 1930s and 1940s, the concept was expanded to the separation of signals from noise, characterized by their power spectral densities. Kolmogorov and Wiener used this statistical characterization to form an optimal estimate of the signal given the sum of the signal and noise. With the Kalman filter, also called *Linear Least Mean Squares Estimator* [2], the term has taken on a broader meaning that goes beyond the original idea of separating mixture components. It also involves the solution of an inversion problem, in which the relationship between the measurable variables and the variables of interest is inverted, with the independent variables estimated as functions of the dependent (measurable) variables. These variables of interest can also be dynamic and partially predictable.

2.1 Least Mean Square Filter

The first method for forming an *optimal* estimate from noisy data is the *method of least squares*. Attributed to Carl Friedrich Gauss (1777-1855), but already discovered and used before him, it was the first formal method dealing with measurement errors.

Ideally, in absence of noise, a measurement \mathbf{z} can be seen as a transformation \mathbf{H} applied on the real state vector \mathbf{x} :

$$\begin{bmatrix} z_1 \\ z_2 \\ \vdots \\ z_n \end{bmatrix} = \begin{bmatrix} h_{11} & h_{12} & \dots & h_{1m} \\ h_{21} & h_{22} & \dots & h_{2m} \\ \vdots & \vdots & \ddots & \vdots \\ h_{n1} & h_{n2} & \dots & h_{nm} \end{bmatrix} \begin{bmatrix} \hat{x}_1 \\ \hat{x}_2 \\ \vdots \\ \hat{x}_n \end{bmatrix} \quad (2.1)$$

or

$$\mathbf{z} = \mathbf{H}\mathbf{x} \quad (2.2)$$

Then, the aim of a Least-Mean-Squares Estimator (LMSE) is minimizing the “estimated measurement error”, or, equivalently, its square:

$$\begin{aligned} \epsilon^2(\hat{\mathbf{x}}) &= |\mathbf{H}\hat{\mathbf{x}} - \mathbf{z}|^2 \\ &= \sum_{i=1}^n \left[\sum_{j=1}^m h_{ij}\hat{x}_j - z_i \right]^2 \end{aligned} \quad (2.3)$$

where $\hat{\mathbf{x}}$ is the state estimate. It is a continuously differentiable function of the n unknowns $\hat{x}_1, \hat{x}_2, \dots, \hat{x}_n$.

Consequently it will achieve its minimum value where all its derivatives with respect to the \hat{x}_k are zero. Therefore, there are n such equations of the form:

$$\begin{aligned} 0 &= \frac{\partial \epsilon^2}{\partial \hat{x}_k} \\ &= \sum_{i=1}^n h_{ik} \left[\sum_{j=1}^m h_{ij}\hat{x}_j - z_i \right] \\ &= 2\mathbf{H}^T [\mathbf{H}\hat{\mathbf{x}} - \mathbf{z}] \\ &= 2\mathbf{H}^T \mathbf{H}\hat{\mathbf{x}} - 2\mathbf{H}^T \mathbf{z} \end{aligned} \quad (2.4)$$

since:

$$\sum_{j=1}^m h_{ij}\hat{x}_j - z_i = \{\mathbf{H}\hat{\mathbf{x}} - \mathbf{z}\}_i \quad (2.5)$$

As a result, the Least-Mean-Squares (LMS) solution to the minimization problem is given by the equation:

$$\hat{\mathbf{x}} = (\mathbf{H}^T \mathbf{H})^{-1} \mathbf{H}^T \mathbf{z} \quad (2.6)$$

$$\mathcal{G} = \mathbf{H}^T \mathbf{H} \quad (2.7)$$

provided that the so-called *Gramian matrix* \mathcal{G} (2.7) is *non-singular*, i.e. invertible. On the other hand, in general, the more redundant measurements there are, the more accurate is the estimation.

2.1.1 LMS Position estimation

One possible way to solve for the Position, Velocity and Timing (PVT), is to use the LMS algorithm, not applied a single time, but iterated in order to provide a more precise solution: at each iteration, the estimated position is expected to be closer to the real user location.

For PVT problems, the LMS equation becomes:

$$\Delta \hat{\mathbf{x}} = (\mathbf{H}^T \mathbf{H})^{-1} \mathbf{H}^T \Delta \hat{\boldsymbol{\rho}} \quad (2.8)$$

At each iteration, a predicted position-state estimate is used to calculate the Observation matrix H and solve the LMS equation. The result represents the increment to the prediction for obtaining the final position-state estimate, which will be used as prediction at the next iteration.

Algorithm 1 Iterative LMS algorithm.

```

 $\hat{x}_n^0 = [0]$ 
for iteration  $k$  do
     $\Delta \hat{\rho}_n^k = \hat{\rho}_n^k - \rho_n$ 
     $\Delta \hat{x}_n^k = [(H_n^k)^T H_n^k]^{-1} (H_n^k)^T \Delta \hat{\rho}_n^k$ 
     $\hat{x}_n^k = \hat{x}_n^{k-1} + \Delta \hat{x}_n^k$ 
end for
    
```

The estimated position-state is composed of the three position coordinates in the reference frame and the clock bias term:

$$\hat{\mathbf{x}}_n^k = [\hat{x}_n^k, \hat{y}_n^k, \hat{z}_n^k, \hat{b}_n^k] \quad (2.9)$$

The Observation matrix H , is derived as linearisation of the non-linear problem:

$$\mathbf{H}_n^k = \begin{bmatrix} a_{x,1} & a_{y,1} & a_{z,1} & 1 \\ a_{x,2} & a_{y,2} & a_{z,2} & 1 \\ a_{x,3} & a_{y,3} & a_{z,3} & 1 \\ a_{x,4} & a_{y,4} & a_{z,4} & 1 \end{bmatrix} \quad (2.10)$$

Where $[a_{x,j}, a_{y,j}, a_{z,j}]$ is the unitary vector steering from the predicted position $\hat{\mathbf{x}}_n^k$ to the j -th satellite, whose position is assumed to be known, and that is away from the prediction by a length $\hat{r}_{j,n}$.

$$\hat{r}_{j,n} = \sqrt{(x_{j,n} - \hat{x}_n^k)^2 + (y_{j,n} - \hat{y}_n^k)^2 + (z_{j,n} - \hat{z}_n^k)^2} \quad (2.11)$$

$$\begin{aligned} a_{x,j} &= \frac{x_{j,n} - \hat{x}_n^k}{\hat{r}_{j,n}} \\ a_{y,j} &= \frac{y_{j,n} - \hat{y}_n^k}{\hat{r}_{j,n}} \\ a_{z,j} &= \frac{z_{j,n} - \hat{z}_n^k}{\hat{r}_{j,n}} \end{aligned}$$

2.1.2 LMS Velocity estimation

As for the estimation of velocity-state, modern receivers rely on Doppler measurements, namely, the frequency shift due to the relative motion of the satellites with respect to the receiver. The frequency measured by the receiver f_R is linked to the transmitted one f_T through the Doppler equation [3]:

$$f_R = f_T \left[1 - \frac{1}{c} (\mathbf{v}_S - \mathbf{v}) \cdot \frac{\mathbf{r}_S - \mathbf{r}}{|\mathbf{r}_S - \mathbf{r}|} \right] \quad (2.12)$$

where:

- $\mathbf{r}_S = [x_S, y_S, z_S]$ is the satellite position vector
- $\mathbf{r} = [x, y, z]$ is the receiver position vector (assumed known)
- $\frac{\mathbf{r}_S - \mathbf{r}}{|\mathbf{r}_S - \mathbf{r}|}$ is the unit vector pointing from the receiver to the satellite

The scalar product $(\mathbf{v}_S - \mathbf{v}) \cdot \frac{\mathbf{r}_S - \mathbf{r}}{|\mathbf{r}_S - \mathbf{r}|}$, represents the projection of the relative velocity vector on the direction from the receiver to the satellite, namely, the *pseudorange rate*.

$$f_R = f_T \left[1 - \frac{1}{c} (\mathbf{v}_S - \mathbf{v}) \cdot \frac{\mathbf{r}_S - \mathbf{r}}{|\mathbf{r}_S - \mathbf{r}|} \right] \quad (2.13)$$

The Doppler shift is therefore given by:

$$f_R - f_T = -\frac{f_T}{c} (\mathbf{v}_S - \mathbf{v}) \cdot \frac{\mathbf{r}_S - \mathbf{r}}{|\mathbf{r}_S - \mathbf{r}|} = -\frac{f_T}{c} \dot{\rho} \quad (2.14)$$

However, the measured pseudorange rate must take into account the drifts of the clock in receiver and satellite. Assuming to be able to compensate for the satellite clock drift, the measured range rate will be:

$$\tilde{\rho} = \dot{\rho} - c\delta\dot{t}_R \quad (2.15)$$

By expanding the scalar product and rearranging the equation:

$$\tilde{\dot{\rho}} - \mathbf{v}_S \cdot \frac{\mathbf{r}_S - \mathbf{r}}{|\mathbf{r}_S - \mathbf{r}|} = -\mathbf{v} \cdot \frac{\mathbf{r}_S - \mathbf{r}}{|\mathbf{r}_S - \mathbf{r}|} - c\delta\dot{t}_R \quad (2.16)$$

We can define the quantities:

$$d = |\mathbf{r}_S - \mathbf{r}| \quad (2.17)$$

$$\zeta_{\dot{\rho}} = \tilde{\dot{\rho}} - \mathbf{v}_S \cdot \frac{\mathbf{r}_S - \mathbf{r}}{|\mathbf{r}_S - \mathbf{r}|} \quad (2.18)$$

such that:

$$\begin{aligned} \zeta_{\dot{\rho}} &= -\mathbf{v} \cdot \frac{\mathbf{r}_S - \mathbf{r}}{|\mathbf{r}_S - \mathbf{r}|} - c\delta\dot{t}_R \\ &= \frac{x - x_S}{d}v_x + \frac{y - y_S}{d}v_y + \frac{z - z_S}{d}v_z - c\delta\dot{t}_R \end{aligned} \quad (2.19)$$

We now have four unknowns which can be solved by using measurements from four (at least) satellites, as done before.

$$\zeta_{\dot{\rho}} = \mathbf{H}\mathbf{g} \quad (2.20)$$

$$\begin{bmatrix} \zeta_{\dot{\rho},1} \\ \zeta_{\dot{\rho},2} \\ \zeta_{\dot{\rho},3} \\ \zeta_{\dot{\rho},4} \end{bmatrix} = \begin{bmatrix} a_{x,1} & a_{y,1} & a_{z,1} & 1 \\ a_{x,2} & a_{y,2} & a_{z,2} & 1 \\ a_{x,3} & a_{y,3} & a_{z,3} & 1 \\ a_{x,4} & a_{y,4} & a_{z,4} & 1 \end{bmatrix} \begin{bmatrix} v_x \\ v_y \\ v_z \\ -c\delta\dot{t}_R \end{bmatrix} \quad (2.21)$$

and the solutions for velocity and time drift are obtained as:

$$\mathbf{g} = \mathbf{H}^{-1}\zeta_{\dot{\rho}} \quad (2.22)$$

2.1.3 LMS Estimation error

The quality of estimates depends on the satellite geometry as well as on the error in the pseudorange estimation, as can be derived from Equations (2.8) and (2.22). The covariance of the LMS solution is defined as:

$$\begin{aligned} cov(\Delta\mathbf{x}) &= E\{(\mathbf{H}^T\mathbf{H})^{-1}\mathbf{H}^T\Delta\rho\Delta\rho^T\mathbf{H}(\mathbf{H}^T\mathbf{H})^{-1}\} \\ &= (\mathbf{H}^T\mathbf{H})^{-1}\mathbf{H}^T cov(\Delta\rho)\mathbf{H}(\mathbf{H}^T\mathbf{H})^{-1} \\ &= (\mathbf{H}^T\mathbf{H})^{-1} cov(\Delta\rho) \\ &= \mathbf{G} \cdot \sigma_{URE}^2 \end{aligned} \quad (2.23)$$

In particular, the *standard deviation of the positioning error* can be obtained as:

$$\sigma_x = \sqrt{\sigma_x^2 + \sigma_y^2 + \sigma_z^2 + \sigma_b^2} = GDOP \cdot \sigma_{URE}^2 \quad (2.24)$$

The *Geometric Dilution Of Precision* (GDOP) is defined as:

$$GDOP = \sqrt{\text{tr}\{\mathbf{G}\}} \quad (2.25)$$

where:

$$\mathbf{G} = (\mathbf{H}^T \mathbf{H})^{-1} \quad (2.26)$$

It is greater than or equal to 1, depending on the geometry of the visible satellites. The more the satellites are distributed around the receiver, the smaller the GDOP. The condition GDOP=1 could be reached if the satellite were distributed in a tetrahedron around the receiver, which would have to stand at its barycenter.

This dependency (2.24) is a bottleneck for the LMS filter that, despite being quite good as a first approximation, can not achieve good performance in space applications. As a matter of fact, the farther the receiver is from Earth, the worse the distribution of satellites around the receiver itself, and so the larger the GDOP. In conclusion, the positioning error for an LMS filter in space application is expected to be very large.

2.2 Kalman Filter

Initially called *Linear Least Mean Squares Estimator (LLSME)*, the Kalman Filter (KF) minimizes the mean-squared estimation error for a linear stochastic system using noisy linear sensors. It is also called *Linear Quadratic Estimator (LQE)* because it minimizes a quadratic function of estimation error for a linear dynamic system with white measurement and disturbance noise.

For some applications, it is not possible or desirable to measure every variable that you want to control, and the KF provides the mathematical framework for inferring the unmeasured variables from indirect and noisy measurements. The KF is also used for predicting the likely future courses of dynamic systems that people are not likely to control such as the trajectories of celestial bodies. It has become a universal tool for integrating different sensors and/or data collection systems into an overall optimal solution.

The KF uses a parametric characterization of the probability distribution of its estimation errors in determining the optimal filtering gains, and these parameters may be used in assessing its performance as a function of the design parameters of an estimation system, such as types of sensors to be used, locations and orientations of the various sensor types w.r.t. the system to be estimated, allowable noise

characteristics of the sensors, prefiltering methods for smoothing sensor noise, data sampling rates for the various sensor types or level of model simplification to reduce the required level of estimation accuracy.

We use KF to make an *educated guess*, about what the system is going to do next in any place where we have uncertain information about some dynamic system. Its main advantages are:

- it can predict the next state based on the previous only, with no need for data history
- even with a lot of noise, KF is able to produce good results
- it is computationally very fast, making it well suitable for real-time problems

The Kalman filter is an iterative process divided into two steps:

- 1) **Prediction:** the KF predicts the new state from the initial values and then predicts the uncertainty of the prediction according to the various process noise present in the system.
- 2) **Update:** the KF takes the actual measured values and compares them to the predicted ones and weighting the choice between the predicted and the measured quantities, calculating the *Kalman Gain*. Based upon the decision made by the Kalman gain the filter calculates the new value and new uncertainty. This output from the update step is again fed back to the prediction step and the process continues till the difference between the predicted value and the measured value tends to converge to zero.

The operating principle of the KF, depicted in Figure 2.1, where:

- \mathbf{F} or Φ is the *dynamic coefficient matrix* of a continuous linear differential equation defining a dynamic system.

This matrix describes how the system's state evolves over time. It maps the state at time t to the state at time $t + 1$.

- \mathbf{H} is the *measurement sensitivity/observation matrix*, defining the linear relationship between the state of the dynamic system and measurements that can be made.

This matrix describes how the system's state is related to the measurements that are available. It maps the state at time t to the predicted measurement at time $t + 1$.

- \mathbf{Q} is the *covariance matrix of process noise* in the system state dynamics.

This matrix describes the covariance of the process noise, which is assumed to be additive and Gaussian. It is used to model the uncertainty in the state transition equation and is typically estimated from prior knowledge of the system's dynamics.

- \mathbf{P} is the *covariance matrix of state estimation uncertainty*.

This matrix describes the uncertainty in the estimated state of the system. It represents the covariance of the error between the estimated state and the true state. \mathbf{P} is updated iteratively as new measurements become available, and it converges to the steady-state value that represents the minimum possible error covariance given the model and measurements.

- \mathbf{R} is the *covariance matrix of observational measurement uncertainty*.

This matrix describes the covariance of the measurement noise, which is assumed to be additive and Gaussian. It is used to model the uncertainty in the measurement equation and is typically estimated from calibration or prior knowledge of the measurement system.

- \mathbf{K} is the *Kalman gain matrix*.

This matrix determines how much weight should be given to the model prediction versus the measurement data when updating the state estimate. It is a function of the error covariance matrix (\mathbf{P}), which represents the uncertainty in the estimate, and the measurement noise covariance matrix (\mathbf{R}), which represents the uncertainty in the measurements.

2.2.1 Linearized Kalman filter

In a standard Kalman filter, it's assumed that the relationship between the measurement vector (\mathbf{z}) and the state vector (\mathbf{x}) is linear. However, this isn't always accurate for real-world systems. Some applications processing range measurements like a Global Navigation Satellite System (GNSS) navigation filter, require a highly nonlinear measurement model. Furthermore, the system model is also assumed to be linear in the standard KF (i.e., $\dot{\mathbf{x}}$ is a linear function of \mathbf{x}). Closed-loop correction of the system using the state estimates can often be used to maintain a linear approximation in the system model. However, it is not always possible to perform the necessary feedback to the system.

The Extended Kalman Filter (EKF) is a nonlinear version of the KF. The system matrix \mathbf{F} and the measurement matrix \mathbf{H} , can be replaced in the state propagation and update equations by nonlinear functions of the state vector, respectively $\mathbf{f}(\mathbf{x})$

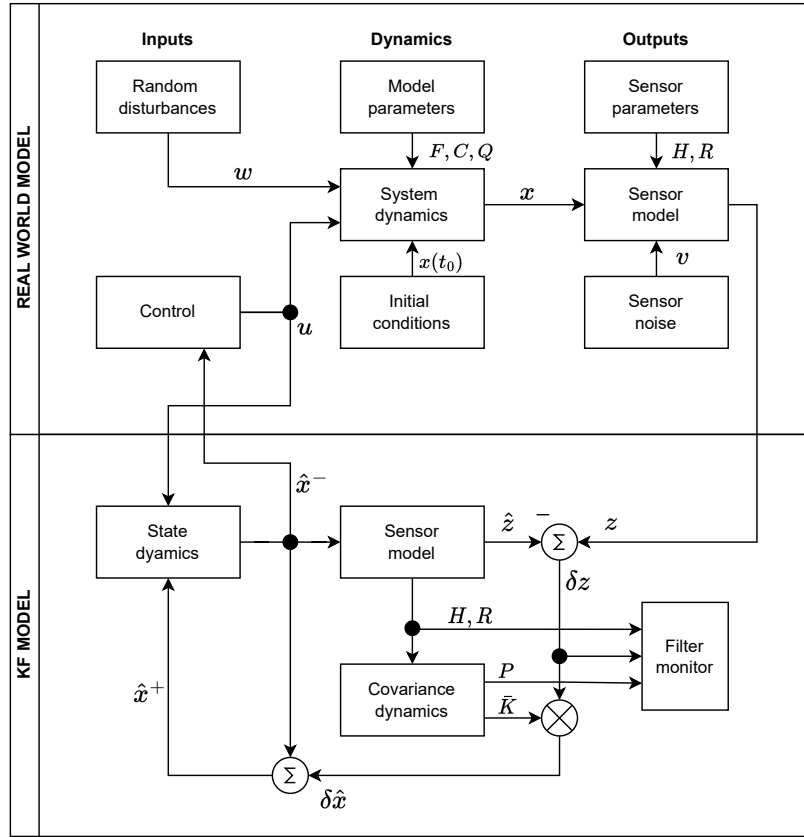


Figure 2.1: KF block diagram.

and $\mathbf{h}(\mathbf{x})$. The process to be estimated and the associated relationship may be written in the form:

$$\dot{\mathbf{x}} = \mathbf{f}(\mathbf{x}, \mathbf{u}_d, t) + \mathbf{u}(t) \quad (2.27)$$

$$\mathbf{z} = \mathbf{h}(\mathbf{x}, t) + \mathbf{v}(t) \quad (2.28)$$

where \mathbf{u}_d is a deterministic forcing function and u and v are white noise processes with zero cross-correlation. Nonlinearity may enter into the problem either in the dynamics of the process or in the measurement relationship.

Let us assume that an approximate trajectory $\mathbf{x}^*(t)$ may be determined by some means, let it be the “nominal trajectory” (Fig. 2.2). The actual trajectory may be written as:

$$\mathbf{x}(t) = \mathbf{x}^*(t) + \Delta\mathbf{x}(t) \quad (2.29)$$

Equations (2.27) and (2.28) become:

$$\dot{\mathbf{x}}^* + \Delta \dot{\mathbf{x}} = \mathbf{f}(\mathbf{x}^* + \Delta \mathbf{x}, \mathbf{u}_d, t) + \mathbf{u}(t) \quad (2.30)$$

$$\mathbf{z} = \mathbf{h}(\mathbf{x}^* + \Delta \mathbf{x}, t) + \mathbf{v}(t) \quad (2.31)$$

If $\Delta \mathbf{x}$ is small enough, we can approximate \mathbf{f} and \mathbf{h} functions with Taylor's series expansions, retaining only first-order terms:

$$\dot{\mathbf{x}}^* + \Delta \dot{\mathbf{x}} \approx \mathbf{f}(\mathbf{x}^*, \mathbf{u}_d, t) + \left[\frac{\partial \mathbf{f}}{\partial \mathbf{x}} \right]_{\mathbf{x}=\mathbf{x}^*} \cdot \Delta \mathbf{x} + \mathbf{u}(t) \quad (2.32)$$

$$\mathbf{z} \approx \mathbf{h}(\mathbf{x}^*, t) + \left[\frac{\partial \mathbf{h}}{\partial \mathbf{x}} \right]_{\mathbf{x}=\mathbf{x}^*} \cdot \Delta \mathbf{x} + \mathbf{v}(t) \quad (2.33)$$

where:

$$\frac{\partial \mathbf{f}}{\partial \mathbf{x}} = \begin{bmatrix} \frac{\partial f_1}{\partial x_1} & \frac{\partial f_1}{\partial x_2} & \cdots \\ \frac{\partial f_2}{\partial x_1} & \frac{\partial f_2}{\partial x_2} & \cdots \\ \vdots & \vdots & \ddots \end{bmatrix}; \quad \frac{\partial \mathbf{h}}{\partial \mathbf{x}} = \begin{bmatrix} \frac{\partial h_1}{\partial x_1} & \frac{\partial h_1}{\partial x_2} & \cdots \\ \frac{\partial h_2}{\partial x_1} & \frac{\partial h_2}{\partial x_2} & \cdots \\ \vdots & \vdots & \ddots \end{bmatrix} \quad (2.34)$$

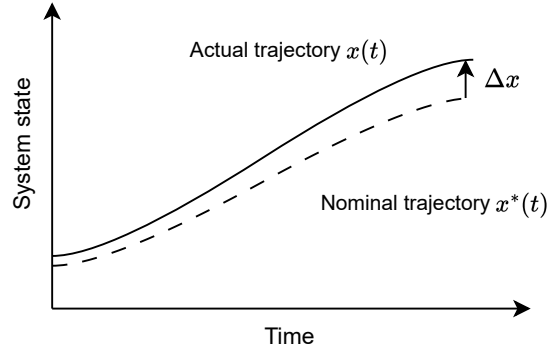


Figure 2.2: Nominal and actual trajectories for a Linearized KF.

A typical choice is to set:

$$\dot{\mathbf{x}}^* = \mathbf{f}(\mathbf{x}^*, \mathbf{u}_d, t) \quad (2.35)$$

Substituting this into Equation (2.32), we obtain the **linearized model**:

- linearized dynamics

$$\Delta \dot{\mathbf{x}} = \left[\frac{\partial \mathbf{f}}{\partial \mathbf{x}} \right]_{\mathbf{x}=\mathbf{x}^*} \cdot \Delta \mathbf{x} + \mathbf{u}(t) \quad (2.36)$$

- linearized measurement equation

$$[z - \mathbf{h}(\mathbf{x}^*, t)] = \left[\frac{\partial \mathbf{h}}{\partial \mathbf{x}} \right]_{\mathbf{x}=\mathbf{x}^*} \cdot \Delta \mathbf{x} + \mathbf{v}(t) \quad (2.37)$$

Note that the “measurement” in the linear model is the actual measurement minus that predicted by the nominal trajectory in the absence of noise. Also, the equivalent F and H matrices are obtained by evaluating the partial derivative matrices (2.34) along the nominal trajectory.

2.2.2 Extended Kalman Filter

The EKF is similar to a linearized Kalman filter except that the linearization takes place about the filter’s estimated trajectory rather than a precompiled nominal trajectory, as depicted in Figure 2.3. That is, the partial derivatives of (2.34) are evaluated along a trajectory that has been updated with the filter’s estimates.

It should be remembered that the basic state variables in a linearized Kalman filter are incremental quantities, and not total quantities such as position, velocity, and so forth.

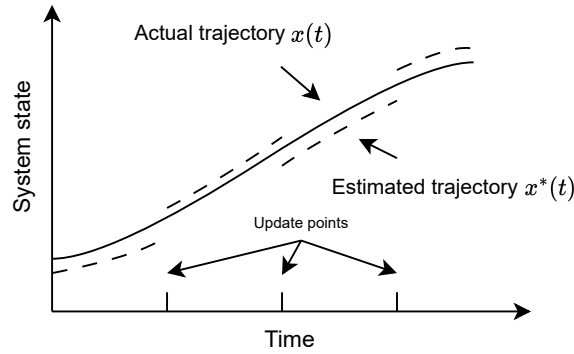


Figure 2.3: Estimated and actual trajectories for a Linearized KF.

The basic linearized measurement equation (2.37) can be rewritten as:

$$z - \mathbf{h}(\mathbf{x}^*) = \mathbf{H} \Delta \mathbf{x} + \mathbf{v} \quad (2.38)$$

Note that this quantity represent the “measurement” presented in the KF, rather than the total measurement \mathbf{z} . Therefore, the (incremental) estimate update at time t_k is:

$$\Delta \hat{\mathbf{x}}_k = \Delta \hat{\mathbf{x}}_k^- + \mathbf{K}_k \underbrace{[z_k - \mathbf{h}(\mathbf{x}_k^*) - \mathbf{H}_k \Delta \hat{\mathbf{x}}_k^-]}_{\text{Inc. meas}} \quad (2.39)$$

Summing the $\mathbf{h}(\mathbf{x}_k^*)$ term with $\mathbf{H}_k \Delta \hat{\mathbf{x}}_k^-$ we obtain the predictive estimate of the measurement, $\hat{\mathbf{z}}_k^-$.

We can define:

$$\text{Measurement residual} = (\mathbf{z}_k - \hat{\mathbf{z}}_k^-) \quad (2.40)$$

Rewriting Equation (2.39) adding \mathbf{x}_k^* to both sides:

$$\underbrace{\mathbf{x}_k^* + \Delta \hat{\mathbf{x}}_k}_{\hat{\mathbf{x}}_k} = \underbrace{\mathbf{x}_k^* + \Delta \hat{\mathbf{x}}_k^-}_{\hat{\mathbf{x}}_k^-} + \mathbf{K}_k (\mathbf{z}_k - \hat{\mathbf{z}}_k^-) \quad (2.41)$$

$$\hat{\mathbf{x}}_k = \hat{\mathbf{x}}_k^- + \mathbf{K}_k (\mathbf{z}_k - \hat{\mathbf{z}}_k^-) \quad (2.42)$$

Equation (2.42) is the familiar linear estimate update equation written in terms of total quantities. It simply says that we correct the *a-priori estimate* by adding the measurement residual appropriately weighted by the Kalman gain \mathbf{K}_k . Note that after the update is made in the extended Kalman filter, the incremental $\Delta \hat{\mathbf{x}}_k$ is reduced to zero. Its projection to the next step is then trivial. The only nontrivial projection is to project $\hat{\mathbf{x}}_k$ to $\hat{\mathbf{x}}_{k+1}^-$. This will be the solution of the nonlinear differential Equation (2.27) at $t = t_{k+1}$, subject to the initial condition $\mathbf{x} = \hat{\mathbf{x}}_k$ at t_k .

Note that the additive white noise forcing function $\mathbf{u}(t)$ is zero in the projection step, but the deterministic \mathbf{u}_d is included in the \mathbf{f} function. Once $\hat{\mathbf{x}}_{k+1}^-$ is determined, the predictive measurement $\hat{\mathbf{z}}_{k+1}^-$ can be formed as $\mathbf{h}(\hat{\mathbf{x}}_{k+1}^-)$, and the measurement residual at t_{k+1} is formed as the difference $(\mathbf{z}_{k+1} - \hat{\mathbf{z}}_{k+1}^-)$. The filter is then ready to go through another recursive loop.

Getting the EKF started

The EKF might diverge when the reference about which the linearization takes place is poor. The most common situation of this type occurs at the starting point of the recursive process. Usually, the *a-priori* information about the true state of the system is poor. This causes a large error in $\hat{\mathbf{x}}_0^-$, and forces \mathbf{P}_0 to be large.

Two problems may arise when getting the EKF started:

1. A very large \mathbf{P}_0^- combined with low-noise measurements at the first step will cause the \mathbf{P} matrix to “jump” from a very large value to a small value in one step. In principle, this is permissible. However, this can lead to numerical problems. A non-positive-definite \mathbf{P} matrix at any point in the recursive process usually leads to divergence.
2. The initial $\hat{\mathbf{x}}_0^-$ is presumably the best estimate of \mathbf{x} prior to receiving any measurement information, and thus, it is used as the reference for linearization.

If the error in $\hat{\mathbf{x}}_0^-$ is large, the first-order approximation used in the linearization will be poor, and divergence may occur, even with perfect arithmetic.

Concerning problem 1, the filter should be designed to preserve symmetry and the positive definiteness of the \mathbf{P} matrix. One way to achieve this is using the following formulation for \mathbf{P}_k :

$$\hat{\mathbf{P}}_k = (\mathbf{I} - \mathbf{K}_k \mathbf{H}_k) \hat{\mathbf{P}}_k^- (\mathbf{I} - \mathbf{K}_k \mathbf{H}_k)^T + \mathbf{K}_k \mathbf{R}_k \mathbf{K}_k^T \quad (2.43)$$

Problem 2 is more subtle than problem 1. Even with perfect arithmetic, poor linearization can cause a poor $\hat{\mathbf{x}}_0^-$ to be updated into an even poorer a posteriori estimate, which in turn gets projected on ahead, and so forth [2]. For this work, the initialization was made through the result coming from the LMS solution. The EKF is described by the following algorithm.

Algorithm 2 EKF algorithm.

for iteration \mathbf{k} do

$\hat{\mathbf{x}}_k^- = \Phi_k \hat{\mathbf{x}}_{k-1}^+ + \mathbf{B}_k \mathbf{u}_k$	▷ PREDICTION
$\hat{\mathbf{P}}_k^- = \Phi_k \hat{\mathbf{P}}_{k-1}^+ \Phi_k^T + \mathbf{Q}_k$	▷ a-priori state
	▷ covariance matrix of the a-priori state
	▷ UPDATE
$\tilde{\mathbf{y}}_k = \mathbf{z}_k - \mathbf{H}_k \hat{\mathbf{x}}_k^-$	▷ innovation vector
$\mathbf{K}_k = \hat{\mathbf{P}}_k^- \mathbf{H}_k^T (\mathbf{H}_k \hat{\mathbf{P}}_k^- \mathbf{H}_k^T + \mathbf{R}_k)^{-1}$	▷ Kalman gain
$\hat{\mathbf{x}}_k^+ = \hat{\mathbf{x}}_k^- + \mathbf{K}_k \tilde{\mathbf{y}}_k$	▷ a-posteriori state
$\hat{\mathbf{P}}_k = (\mathbf{I} - \mathbf{K}_k \mathbf{H}_k) \hat{\mathbf{P}}_k^- (\mathbf{I} - \mathbf{K}_k \mathbf{H}_k)^T + \mathbf{K}_k \mathbf{R}_k \mathbf{K}_k^T$	▷ a-posteriori state
	▷ covariance matrix

end for

2.2.3 Dynamic model for position states

In the Position-Velocity (PV) model illustrated in Figure 2.4, each spatial dimension has two degrees of freedom, one of position and the other of velocity.

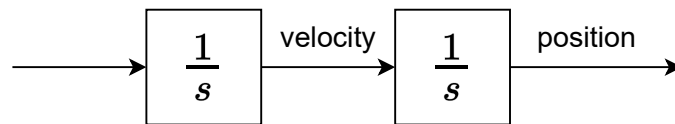


Figure 2.4: PV model.

The PV dynamic process can be described by:

$$\begin{bmatrix} \dot{x}_1 \\ \dot{x}_2 \\ \dot{x}_3 \\ \dot{x}_4 \\ \dot{x}_5 \\ \dot{x}_6 \\ \dot{x}_7 \\ \dot{x}_8 \end{bmatrix} = \begin{bmatrix} 0 & 0 & 0 & 0 & 1 & 0 & 0 & 0 \\ 0 & 0 & 0 & 0 & 0 & 1 & 0 & 0 \\ 0 & 0 & 0 & 0 & 0 & 0 & 1 & 0 \\ 0 & 0 & 0 & 0 & 0 & 0 & 0 & 1 \\ 0 & 0 & 0 & 0 & 0 & 0 & 0 & 0 \\ 0 & 0 & 0 & 0 & 0 & 0 & 0 & 0 \\ 0 & 0 & 0 & 0 & 0 & 0 & 0 & 0 \\ 0 & 0 & 0 & 0 & 0 & 0 & 0 & 0 \end{bmatrix} \begin{bmatrix} x_1 \\ x_2 \\ x_3 \\ x_4 \\ x_5 \\ x_6 \\ x_7 \\ x_8 \end{bmatrix} + \begin{bmatrix} 0 \\ 0 \\ 0 \\ u_f \\ u_1 \\ u_2 \\ u_3 \\ u_g \end{bmatrix} \quad (2.44)$$

where:

- x_1 is the x-component of the position
- x_2 is the y-component of the position
- x_3 is the z-component of the position
- x_4 is the range clock bias error
- x_5 is the x-component of the velocity
- x_6 is the y-component of the velocity
- x_7 is the z-component of the velocity
- x_8 is the range clock drift error
- u_1, u_2, u_3 are white noise driving functions with spectral densities S_p
- u_f is a white noise driving function with spectral density S_f
- u_g is a white noise driving function with spectral density S_g

Being Δt the temporal step between epochs, the transition matrix can be derived as:

$$\Phi = \begin{bmatrix} 1 & 0 & 0 & 0 & \Delta t & 0 & 0 & 0 \\ 0 & 1 & 0 & 0 & 0 & \Delta t & 0 & 0 \\ 0 & 0 & 1 & 0 & 0 & 0 & \Delta t & 0 \\ 0 & 0 & 0 & 1 & 0 & 0 & 0 & \Delta t \\ 0 & 0 & 0 & 0 & 1 & 0 & 0 & 0 \\ 0 & 0 & 0 & 0 & 0 & 1 & 0 & 0 \\ 0 & 0 & 0 & 0 & 0 & 0 & 1 & 0 \\ 0 & 0 & 0 & 0 & 0 & 0 & 0 & 1 \end{bmatrix} \quad (2.45)$$

The process noise covariance matrix can be demonstrated to be:

$$Q = \begin{bmatrix} \frac{S_p \Delta t^3}{3} & 0 & 0 & 0 & \frac{S_p \Delta t^2}{2} & 0 & 0 & 0 \\ 0 & \frac{S_p \Delta t^3}{3} & 0 & 0 & 0 & \frac{S_p \Delta t^2}{2} & 0 & 0 \\ 0 & 0 & \frac{S_p \Delta t^3}{3} & 0 & 0 & 0 & \frac{S_p \Delta t^2}{2} & 0 \\ 0 & 0 & 0 & S_f \Delta t + \frac{S_g \Delta t^3}{3} & 0 & 0 & 0 & \frac{S_g \Delta t^2}{2} \\ \frac{S_p \Delta t^2}{2} & 0 & 0 & 0 & S_p \Delta t & 0 & 0 & 0 \\ 0 & \frac{S_p \Delta t^2}{2} & 0 & 0 & 0 & S_p \Delta t & 0 & 0 \\ 0 & 0 & \frac{S_p \Delta t^2}{2} & 0 & 0 & 0 & S_p \Delta t & 0 \\ 0 & 0 & 0 & \frac{S_g \Delta t^2}{2} & 0 & 0 & 0 & S_g \Delta t \end{bmatrix} \quad (2.46)$$

S_f and S_g represent spectral densities associated with clock bias and drift errors in units of meters. Their measurement units are, respectively, m^2/s and m^2/s^3 .

As for S_p , it is the spectral density of the additive white noise associated with the velocity states, and is measured in m^2/s^3 .

2.2.4 Trajectory-Aware Extended Kalman Filter

The idea behind the Trajectory-Aware Extended Kalman Filter (TA-EKF) is that of using an aiding trajectory to better predict the next state, making faster the filter convergence. The aiding trajectory is the ideal path that the receiver is expected to go through.

At each new iteration, the predicted state is corrected by the estimation error computed as the difference between the last a-posteriori state and its corresponding *aiding state*, coming from the aiding trajectory.

Hence, given an aiding trajectory $\tilde{\mathbf{x}}$ such that, $\tilde{\mathbf{x}}_{k-1}$ is the *aiding state* associated with the filter output $\hat{\mathbf{x}}_{k-1}^+$, for the current epoch k , the predicted state is corrected by the quantity:

$$\boldsymbol{\varepsilon}_{k-1} = \hat{\mathbf{x}}_{k-1}^+ - \tilde{\mathbf{x}}_{k-1} \quad (2.47)$$

Algorithm 3 describes the whole TA-EKF routine.

Algorithm 3 TA-EKF algorithm.

for iteration **k** do

$$\boldsymbol{\varepsilon}_{k-1} = \hat{\boldsymbol{x}}_{k-1}^+ - \tilde{\boldsymbol{x}}_{k-1} \quad \triangleright \text{last estimate error}$$

PREDICTION

$$\hat{\boldsymbol{x}}_k^- = \boldsymbol{\Phi}_k \hat{\boldsymbol{x}}_{k-1}^+ + \boldsymbol{B}_k \boldsymbol{u}_k - \boldsymbol{\varepsilon}_{k-1} \quad \triangleright \text{a-priori state}$$

$$\hat{\boldsymbol{P}}_k^- = \boldsymbol{\Phi}_k \hat{\boldsymbol{P}}_{k-1}^+ \boldsymbol{\Phi}_k^T + \boldsymbol{Q}_k \quad \triangleright \text{covariance matrix of the a-priori state}$$

UPDATE

$$\tilde{\boldsymbol{y}}_k = z_k - \boldsymbol{H}_k \hat{\boldsymbol{x}}_k^- \quad \triangleright \text{innovation vector}$$

$$\boldsymbol{K}_k = \hat{\boldsymbol{P}}_k^- \boldsymbol{H}_k^T (\boldsymbol{H}_k \hat{\boldsymbol{P}}_k^- \boldsymbol{H}_k^T + \boldsymbol{R}_k)^{-1} \quad \triangleright \text{Kalman gain}$$

$$\hat{\boldsymbol{x}}_k^+ = \hat{\boldsymbol{x}}_k^- + \boldsymbol{K}_k \tilde{\boldsymbol{y}}_k \quad \triangleright \text{a-posteriori state}$$

$$\hat{\boldsymbol{P}}_k^+ = (\boldsymbol{I} - \boldsymbol{K}_k \boldsymbol{H}_k) \hat{\boldsymbol{P}}_k^- (\boldsymbol{I} - \boldsymbol{K}_k \boldsymbol{H}_k)^T + \boldsymbol{K}_k \boldsymbol{R}_k \boldsymbol{K}_k^T \quad \triangleright \text{a-posteriori state}$$

covariance matrix

end for

2.2.5 Implementing Kalman Filtering for GNSS Applications

For the PVT problem, the EKF can be implemented so as to work directly with increments.

First of all, an initial prediction is obtained by applying the linearized model, correcting the current position estimate by its drift estimate (no further forcing functions are considered in input):

$$\hat{\boldsymbol{x}}_k^- = \boldsymbol{\Phi} \hat{\boldsymbol{x}}_{k-1}^+ \quad (2.48)$$

For n visible satellites, the Observation matrix \boldsymbol{H} is then defined as linearization about this approximation point:

$$\boldsymbol{U}^k = \begin{bmatrix} a_{x,1} & a_{y,1} & a_{z,1} & 1 \\ a_{x,2} & a_{y,2} & a_{z,2} & 1 \\ a_{x,3} & a_{y,3} & a_{z,3} & 1 \\ \dots & \dots & \dots & \dots \\ a_{x,n} & a_{y,n} & a_{z,n} & 1 \end{bmatrix} \quad (2.49)$$

Where $[a_{x,j}, a_{y,j}, a_{z,j}]$ is the unitary vector steering from the predicted position $\hat{\boldsymbol{x}}_k^-$ to the j -th satellite, whose position is assumed to be known, and that is away from the prediction by a length \hat{r}_j .

$$\hat{r}_j = \sqrt{(x_j - \hat{x}_k^-)^2 + (y_j - \hat{y}_k^-)^2 + (z_j - \hat{z}_k^-)^2} \quad (2.50)$$

$$\begin{aligned} a_{x,j} &= \frac{x_j - \hat{x}_k^-}{\hat{r}_j} \\ a_{y,j} &= \frac{y_j - \hat{y}_k^-}{\hat{r}_j} \\ a_{z,j} &= \frac{z_j - \hat{z}_k^-}{\hat{r}_j} \end{aligned}$$

$$\mathbf{H}^k = \begin{bmatrix} \mathbf{U}^k & \mathbf{0} \\ \mathbf{0} & \mathbf{U}^k \end{bmatrix} \quad (2.51)$$

Concerning the measurement residual, it is computed as the difference between the current measurements \mathbf{z}_k (pseudoranges and pseudorange rates corrected by the estimated bias and drift, respectively) and the nominal measurements calculated with respect to the predicted state $\hat{\mathbf{z}}_k^-$.

$$\text{Measurement residual} = (\mathbf{z}_k - \hat{\mathbf{z}}_k^-) \quad (2.52)$$

where:

$$\hat{\mathbf{z}}_k^- = \begin{bmatrix} \hat{\boldsymbol{\rho}} \\ \hat{\boldsymbol{\rho}} \end{bmatrix} \quad (2.53)$$

$$\hat{\boldsymbol{\rho}} = \begin{bmatrix} \sqrt{\Delta x_1^2 + \Delta y_1^2 + \Delta z_1^2} \\ \sqrt{\Delta x_2^2 + \Delta y_2^2 + \Delta z_2^2} \\ \dots \\ \sqrt{\Delta x_n^2 + \Delta y_n^2 + \Delta z_n^2} \end{bmatrix} = \begin{bmatrix} \hat{r}_1 \\ \hat{r}_2 \\ \dots \\ \hat{r}_n \end{bmatrix} \quad (2.54)$$

$$\hat{\boldsymbol{\rho}} = \begin{bmatrix} (\Delta v_{x,1} \Delta x_1 + \Delta v_{y,1} \Delta y_1 + \Delta v_{z,1} \Delta z_1) / \hat{r}_1 \\ (\Delta v_{x,2} \Delta x_2 + \Delta v_{y,2} \Delta y_2 + \Delta v_{z,2} \Delta z_2) / \hat{r}_2 \\ \dots \\ (\Delta v_{x,n} \Delta x_n + \Delta v_{y,n} \Delta y_n + \Delta v_{z,n} \Delta z_n) / \hat{r}_n \end{bmatrix} \quad (2.55)$$

where:

$$\Delta v_{x,j} = v_{x,j} - \hat{v}_{x,k}^- \quad (2.56)$$

$$\Delta v_{y,j} = v_{y,j} - \hat{v}_{y,k}^- \quad (2.57)$$

$$\Delta v_{z,j} = v_{z,j} - \hat{v}_{z,k}^- \quad (2.58)$$

It is important to note that the observation noise covariance matrix R can be defined differently depending on the specific scenario being tested. For instance, in a terrestrial setting, the weight assigned to a given satellite will be determined by its elevation. However, in a space scenario, such as the one that will be discussed later, the concept of “elevation” is not relevant, and therefore, the criteria used to weigh satellite data will be based on received power.

Once the matrices have been defined, the filter can compute the state increment. In particular, the filter is forced in a manner that results in a state prediction equal to zero for the EKF (which assumes no increment relative to the prediction) or to the correction factor $\boldsymbol{\varepsilon}_{k-1}$ for the TA-EKF. The KF routine subsequently updates the predicted state, which is added to the total state prediction $\hat{\boldsymbol{x}}_k^-$ to update it.

2.2.6 Trajectory-Aware EKF validation testing

The algorithm has been validated by testing it in a terrestrial scenario. Given a ground-truth trajectory, the EKF and TA-EKF filters have been tested on it to compare their performance in a “simple” terrestrial case.

Figure 2.5 illustrates the ground-truth trajectory and the trajectory estimated employing the TA-EKF. Except for an initial manoeuvring phase, where the dynamics of the receiver were rather messy to be suitably linearized, after this, the filter seems to behave very well.

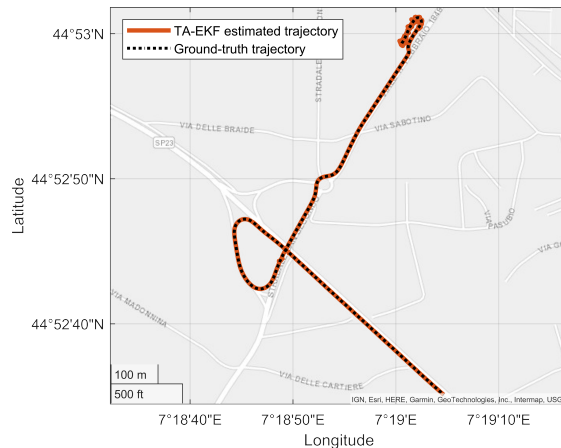


Figure 2.5: Samarcanda dataset. Comparison between the ground-truth trajectory and the estimated one.

For this setting, the observation noise covariance matrix is defined by Equation (2.59), assuming a pseudorange variance of $\sigma_\rho^2 = 400 \text{ m}^2$ and a pseudorange rate variance of $\sigma_{\dot{\rho}}^2 = 3 \text{ m}^2/\text{s}^2$.

$$R = I_{2N} \circ (ru^T) \quad (2.59)$$

The operator (\circ) represents the Hadamard product used to define R as a diagonal matrix.

In particular:

- N is the number of visible satellites
- I_{2N} is the identity matrix of size $2N \times 2N$
- $u = [1, \dots, 1]$ of size $1 \times 2N$
- $r = \{r_i\}$ of size $1 \times 2N$

Equation (2.60) describes the models used for the noise variance of satellite pseudorange ($1 \leq i \leq N$) and pseudorange rate ($N + 1 \leq i \leq 2N$).

$$r_i = \begin{cases} \sigma_\rho^2 / \theta_{el,i}, & \text{if } i \leq N \\ \sigma_{\dot{\rho}}^2 / \theta_{el,i}, & \text{otherwise} \end{cases} \quad (2.60)$$

As for the TA-EKF, it was assumed to have an ideal tool for matching the last PVT estimate to the last true state. Figures 2.6a and 2.6b show a single-realization comparison of the described Kalman filters performance in terms of Empirical Cumulative Distribution Function (ECDF) of the positioning error, summarized in Table 2.1.

Although a single realization can not be considered from a statistical point of view, it is clear that the TA-EKF has great potential, provided that the aiding state is chosen as close as possible to the last true state.

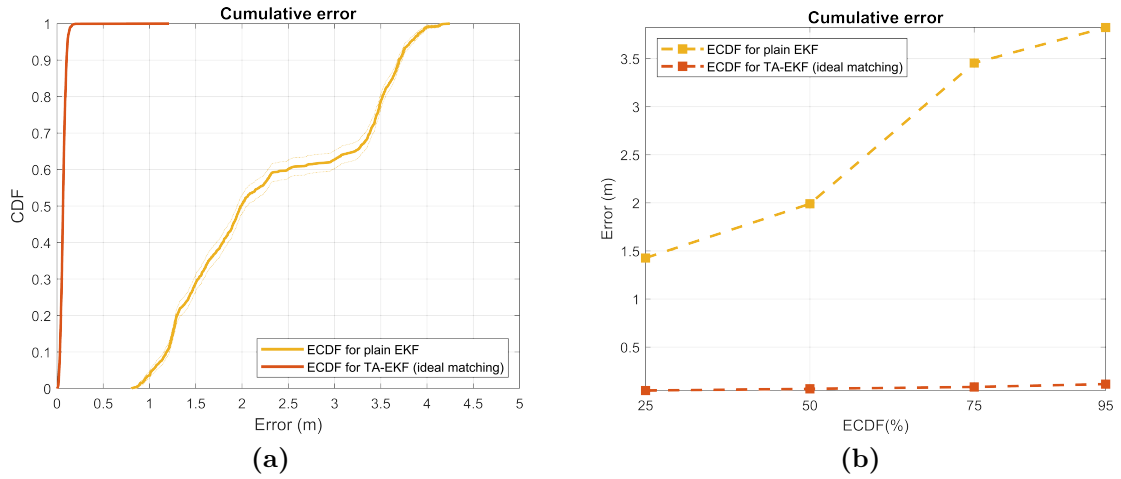


Figure 2.6: ECDF for the positioning error in ECEF-coordinates and Positioning error at 25-th, 50-th, 75-th and 95-th percentiles. Comparison between plain EKF and TA-EKF filters.

Navigation Filter	Error Percentile (m)			
	25-th	50-th	75-th	100-th
Plain EKF	1.43	1.99	3.45	3.82
TA-EKF	0.05	0.07	0.08	0.11

Table 2.1: Positioning error (m) for plain EKF and TA-EKF considering 2000 epochs at 10 Hz.

2.2.7 Choosing the aiding

In principle, the TA-EKF approach would allow a very fast convergence of the filter, even in bad noise conditions, provided it has the best matching between the last PVT estimate and the ground-truth trajectory. Anyway, it is not so trivial to match the last state estimate with its associated *aiding state* belonging to the aiding trajectory.

Assuming that the aiding trajectory perfectly describes the state evolution in time, even with different sample rates, one could calculate the aiding state by interpolating available data, taking into account the elapsed time and receiver motion anomalies that might cause slowdowns and accelerations. The more precise the aiding, the faster will be convergence, therefore further studies should be carried out on this topic.

2.3 Comments on navigation filters

An LMS filter is an algorithm that iteratively adjusts its parameters to minimize the mean squared residuals (difference between nominal measurements calculated from the solution and input measurements). In contrast, a KF is a state-space model that estimates the state of a system based on noisy input measurements, a measurement function and a model of the system dynamics.

LMS filter has some advantages over KFs, such as simplicity of implementation and ease of tuning. However, it assumes all measurement variances are equal (although Weighted Least Mean Square (WLMS) can be used when this is not the case) and no correlation between the measurements.

Kalman filters are often preferred in many applications because they use a model-based approach that allows for incorporating prior knowledge of the system dynamics and incorporating constraints on the system behaviour. This makes them more accurate and robust than LMS filter, especially when the system dynamics are complex. However, KF also requires more computational resources and a more sophisticated system model, which may not be feasible in some applications.

Chapter 3

Simulation framework

Space exploration has always been a topic of fascination for humans. With the advancements in technology, it has become possible to send spacecraft beyond Earth's atmosphere and explore other celestial bodies such as the Moon. However, space exploration comes with its challenges, including the harsh space environment and the need for precise navigation and control systems.

This chapter presents a custom software simulator that emulates the environment of the Global Navigation Satellite System (GNSS) signal that is experienced along the Earth-Moon Transfer Orbit (MTO). In particular, this includes the generation of an Earth-Centered Earth-Fixed (ECEF) environment in which Earth, Moon and Sun are simulated together with Global Positioning System (GPS) and Galileo satellite constellations. The software has been tailored and customized to suit the unique requirements of this specific study.

Then, an MTO navigation is recreated, starting from a ground-truth trajectory, and the GNSS observables that a receiver on board would obtain are generated. Once recreated the environment, different navigation filters have been tested to compare their performances in position estimation.

3.1 Environment background

The whole environment is generated according to the ECEF reference frame, also called *geocentric coordinate system*. It describes the system assuming that Earth is placed at the origin of a Cartesian frame and is still. The motion of objects belonging to the system and moving in it is modelled according to this assumption.

Earth

The Earth is modelled as a sphere of radius:

$$R_E = 6371 \text{ km} \quad (3.1)$$

that will often be used as a “measurement unit” to describe the distance of objects. According to the ECEF reference frame, illustrated in Figure 3.1), the z -axis coincides with the line joining the North and South poles, with positive values increasing northward, whereas the x - y plane represents the equatorial plane. In particular, the x -axis passes through the origin, with positive values increasing toward the prime meridian, whereas the y -axis, as part of the right-handed reference system, is defined accordingly.

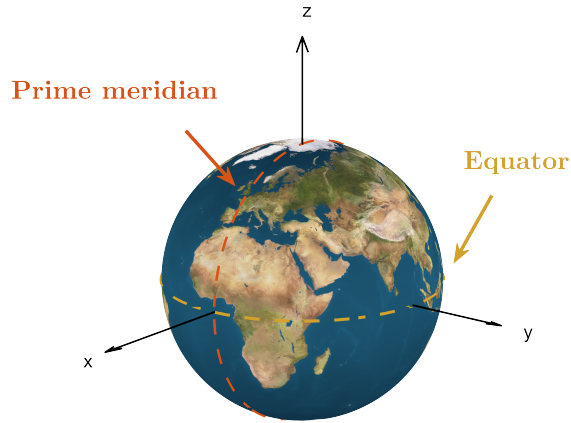


Figure 3.1: ECEF reference frame and Earth representation.

Sun and Moon

Similarly, Sun and Moon are defined as spheres of radii, respectively:

$$R_{sun} = 696340 \text{ km} \quad (3.2)$$

$$R_{moon} = 1737.4 \text{ km} \quad (3.3)$$

Their positions, given a certain date, are obtained thanks to the MATLAB built-in function *planetEphemeris*, which returns the coordinates of a celestial body with respect to a given reference, that, for an ECEF system, is represented by the Earth.

3.2 Receiver

The receiver has been modelled according to the receiver that will be carried by the Lunar GNSS Receiver Experiment (LuGRE) experiment [1]. LuGRE is a NASA-Italian Space Agency project to demonstrate multi-GNSS based navigation and timing in cislunar space and on the Moon using the Firefly Blue Ghost Mission 1 lunar lander. The goal is to receive GPS and Galileo signals on the Moon and to use the data to support the development of GNSS receivers for lunar use.

The LuGRE receiver is designed to collect and process cislunar GPS and Galileo L1/E1 and L5/E5a signals as weak as 20 dB-Hz using high-performance tracking, processing, and navigation algorithms.

3.2.1 Receiver antenna pattern

According to the LuGRE model, the receiver Radio-Frequency (RF) chain consists of a low noise amplifier, filter, and a high-gain antenna with a measured peak boresight gain of 16 dBi at the L1 frequency and the pattern represented in Figure 3.2. The receiver antenna is designed to point toward the ECEF frame’s origin with a radial pointing error of approximately one degree. However, the simulation framework does not consider any pointing errors due to a lack of mission documentation about the error itself.

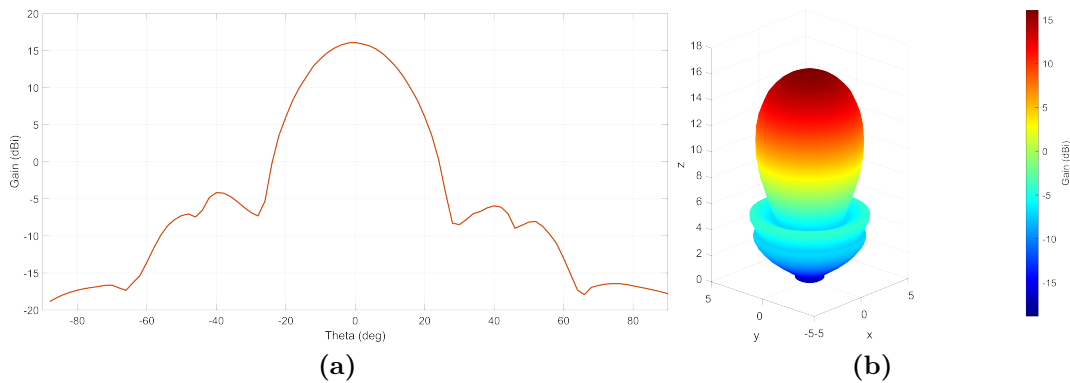


Figure 3.2: LuGRE receiver antenna pattern 2D (a) and 3D (b) representation. Constant for every azimuthal angle.

3.2.2 Receiver clock model

The GNSS receiver clock introduces a timing error that translates into a ranging error which equally affects measurements made to all satellites. This error is generally time-varying and is referred to as user clock bias.

If the satellite measurements are made simultaneously, this receiver clock error is the same on all the measurements. Due to this commonality, the clock error has no effect on positioning accuracy if there are enough satellites to solve for it and so is not included as a source of positioning error. Even so, there are advantages to properly modelling the receiver clock.

A suitable clock model that makes good sense intuitively is a two-state random process model. It simply says that we expect both the oscillator frequency and phase to randomly walk over reasonable spans of time.

From [2], it can be found that:

$$E[x_p^2(\Delta t)] = S_f \Delta t + \frac{S_g \Delta t^3}{3} \quad (3.4)$$

$$E[x_f^2(\Delta t)] = S_g \Delta t \quad (3.5)$$

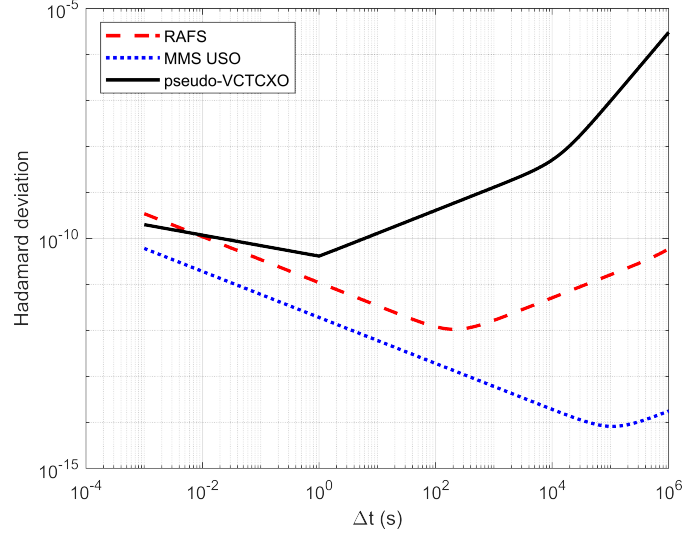
Notice that, in this case, S_f and S_g represent spectral densities for the white noise driving functions associated with clock bias and drift in unit of seconds. Therefore, their measurement units are, respectively, s and $1/s$. When used with clock error in units of meters, like in Equation 2.46, the values must be multiplied by c^2 .

The white noise driving functions associated with the clock phase and frequency errors are determined from the Hadamard variance that characterizes the receiver clock [4]. It was modelled so as to best represent the Voltage Controlled Temperature Compensated Crystal Oscillator (VCTCXO) clock on board the LuGRE receiver [1]. From the experimental plots of the VCTCXO error variances, a parametric function has been deduced according to the Hadamard variance model:

$$\sigma^2 = \frac{10}{3} q_0 \Delta t^{-2} + q_1 \Delta t^{-1} + \frac{1}{6} q_2 \Delta t + \frac{11}{120} q_3 \Delta t^3 \quad (3.6)$$

Figure 3.3 reports three Hadamard deviation plots for three oscillator models: the pseudo-VCTCXO model, similar to the one used in [1], an Magnetospheric MultiScale Ultra Stable Oscillator (MMS USO) and a more stable commercial atomic clock, namely the Spectratime Rubidium Atomic Frequency Standard (RAFS). Their parameters are reported in Table 3.1

Timing Standard	q_0	q_1	q_2	q_3
MMS USO	0	1.2×10^{-22}	1.58×10^{-26}	1×10^{-38}
RAFS	0	3.7×10^{-24}	1.87×10^{-33}	7.56×10^{-59}
pseudo-VCTCXO	0	4×10^{-23}	1×10^{-20}	1×10^{-28}

Table 3.1: Hadamard variance parameters.

Figure 3.3: Hadamard deviation plots of three sample oscillators reported in Table 3.1.

Considering Equations (3.4) and (3.6), and comparing the terms of similar order in Δt , it holds:

$$S_f \Delta t + \frac{S_g \Delta t^3}{3} \sim \frac{1}{6} q_2 \Delta t + \frac{11}{120} q_3 \Delta t^3 \quad (3.7)$$

from which:

$$S_f \sim \frac{1}{6} q_2 \quad (3.8)$$

$$S_g \sim \frac{11}{40} q_3 \quad (3.9)$$

From [2], the average rms value of the clock phase error is given by Eq. (3.10).

$$\bar{x}_{p,rms} = \sqrt{\frac{S_f}{\Delta t} + \frac{S_g \Delta t}{3}} \quad [\text{s}] \quad (3.10)$$

As for the clock drift, the rms drift error variance can be approximated to

$$\sigma_{x_f(\Delta t)}^2 = \frac{S_g}{\Delta t} \quad (3.11)$$

Finally, the overall bias term, in meters, is generated as

$$b = [\bar{x}_{p,rms} + \mathcal{N}(0, \sigma_{x_f(\Delta t)}^2)] \cdot c \quad [\text{m}] \quad (3.12)$$

where c stands for the speed of light.

$$c = 299792458 \text{ m/s} \quad (3.13)$$

3.2.3 Receiver trajectory

Concerning the ground-truth trajectory, it was provided as a sample trajectory that a spacecraft would go through in a journey to the Moon. It contained Earth-Centered Inertial (ECI) J2000 three-dimensional coordinates and velocities, with their associated timestamps. The sample period was of one minute.

To make the trajectory more suitable for simulation purposes, once converted to the ECEF frame, as shown in Figure 3.4, it was interpolated with the *spline* method to keep its nonlinear dynamicity and achieve a sampling period of one second.

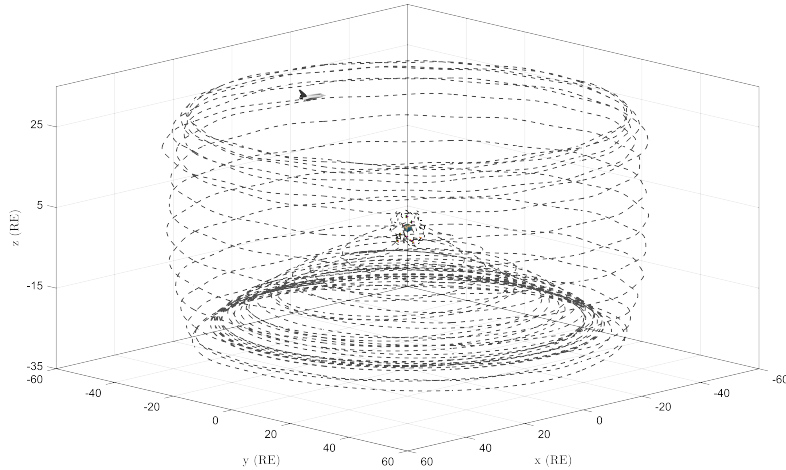


Figure 3.4: Trajectory overview according to the ECEF reference frame with a temporal resolution of 15 minutes between subsequent points.

3.3 GNSS Satellites

Each satellite antenna is oriented according to a relative reference system. However, no unique convention for the labelling of individual spacecraft axes exists. Conversely, distinct frame orientations have been adopted for the various constellations and types of spacecraft depending on the manufacturer’s heritage and preference [5].

To avoid a multitude of attitude descriptions differing only by a permutation of axes, the International GNSS Service (IGS) has adopted a common Body-Fixed (BF) reference, depicted in Figure 3.5:

- the $+z_{IGS}$ -axis is the principal body axis closest to the antenna boresight direction (i.e., the direction of the maximum beam intensity).
- the y_{IGS} -axis is parallel to the rotation axis of the solar panels. The positive y_{IGS} -direction is defined through the corresponding x_{IGS} -axis orientation.
- the $+x_{IGS}$ -axis is chosen such that the $+x_{IGS}$ -panel is permanently sunlit during nominal yaw-steering, while the $-x_{IGS}$ -panel remains dark at all times.

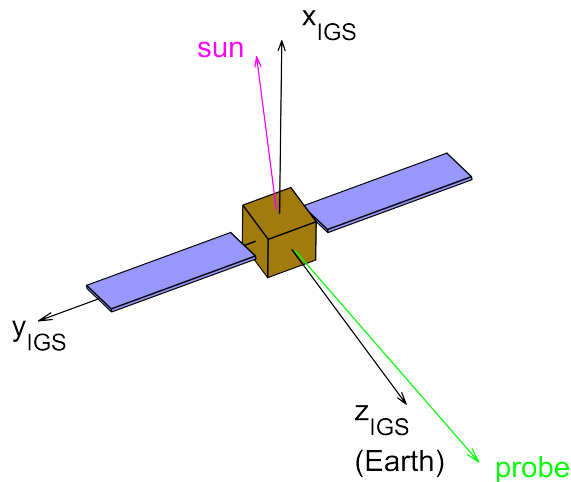


Figure 3.5: Station vehicle IGS reference system with sun and probe (receiver) steering vectors.

As for the origin of each satellite local reference frame, it is located at the centre of mass of its corresponding body, which corresponds to its position.

Two constellations have been considered for this framework: GPS and Galileo. Given the large availability of GPS official documentation provided by Lockheed

Martin, GPS antennas were more straightforward to model. On the other hand, there are no publicly available antenna patterns for Galileo, therefore, some simplifications needed to be made for it.

Three models are considered for GPS: IIR, IIR-M and IIF. The body-fixed coordinate system of the IIF satellites coincides with the IGS convention, whereas for IIR and IIR-M models, the x_{BF} and y_{BF} axes have the same direction but opposite signs with respect to the IGS reference frame.

Concerning Galileo satellites, the BF coordinate system is assumed to coincide with the IGS convention.

All the BF references are summarized in Table 3.2.

	\mathbf{x}_{BF}	\mathbf{y}_{BF}	\mathbf{z}_{BF}
GPS IIR	$-x_{IGS}$	$-y_{IGS}$	z_{IGS}
GPS IIR-M	$-x_{IGS}$	$-y_{IGS}$	z_{IGS}
GPS IIF	x_{IGS}	y_{IGS}	z_{IGS}
Galileo ESA/ESOC	x_{IGS}	y_{IGS}	z_{IGS}

Table 3.2: Satellite antenna body-fixed coordinate system.

3.3.1 GPS constellation

For the GPS constellation, 27 satellites have been generated through the MATLAB built-in function *gnssconstellation*, which produces 27 satellite positions and velocities for a given date and time. The order in which the satellites are generated follows the references in [6], which are reported in Table 3.3.

Antenna patterns

GPS publicly released detailed antenna patterns for satellite models IIR and IIR-M. For the Block IIF satellites (built by Boeing) there have not been released similar data. Logically, the antenna patterns used for IIF Block should be at least as good as the improved antenna pattern, so its pattern is built as the average of all improved antenna patterns [7].

Table 3.3 indicates all matched information related to the ordered satellites provided by MATLAB.

Being the GPS antenna patterns provided by NASA in terms of Directivity, to convert to Gain values, they need to be corrected by the Gain Correction Factor (GCF) provided in [8]. For IIF models, an average GCF of 1 dB is assumed. Figures 3.6, 3.7 and 3.8 depict the GPS satellite antenna Gain patterns that have been reconstructed for the simulation framework.

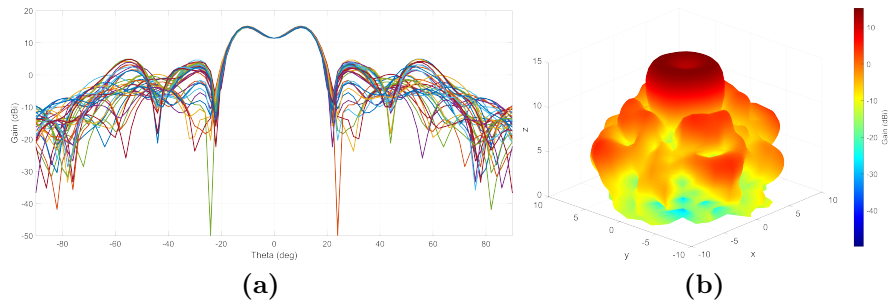


Figure 3.6: GPS IIR model antenna pattern 2D (a) and 3D (b) representation. Azimuthal angle cuts every 10 degrees.

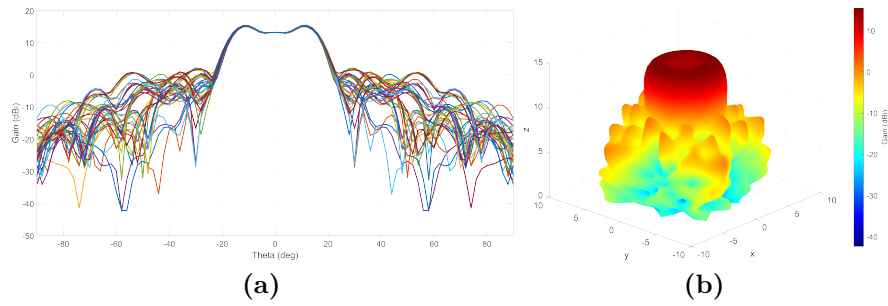


Figure 3.7: GPS IIR-M model antenna pattern 2D (a) and 3D (b) representation. Azimuthal angle cuts every 10 degrees.

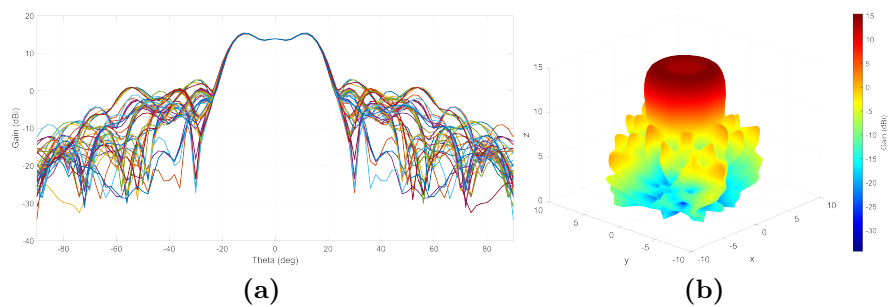


Figure 3.8: GPS IIF model antenna pattern 2D (a) and 3D (b) representation. Azimuthal angle cuts every 10 degrees.

SV no.	Slot ID	Model	SVN	GCF
1	A1	IIF	65	1
2	A2	IIR-M	52	1.2
3	A3	IIF	64	1
4	A4	IIR-M	48	1.4
5	B1F	IIF	71	1
6	B1A	IIR	56	0.7
7	B2	IIF	62	1
8	B3	IIR	44	1.1
9	B4	IIR-M	58	1.3
10	C1	IIR-M	57	1.3
11	C2	IIF	66	1
12	C3	IIF	72	1
13	C4	IIR-M	53	1.4
14	D1	IIR	61	1.2
15	D2F	IIR	46	1
16	D2A	IIF	63	1
17	D3	IIR	45	1.1
18	D4	IIF	67	1
19	E1	IIF	69	1
20	E2	IIF	73	1
21	E3	IIR-M	50	1.3
22	E4	IIR	51	0.7
23	F1	IIF	70	1
24	F2F	IIR	41	0.9
25	F2A	IIR-M	55	1.3
26	F3	IIF	68	1
27	F4	IIR	60	1.3

Table 3.3: Data associated with the GPS-constellation list generated by the framework.

3.3.2 Galileo constellation

Unlike GPS, MATLAB does not provide any direct tool for generating Galileo satellite positions and velocities. However, a Simulink model can be built, to simulate Galileo orbits extrapolating satellite positions and velocities at a given date, similarly to what was done for GPS [9].

Antenna patterns

Concerning Galileo satellites' antenna radiation patterns, the details of which are kept confidential, unofficial Effective Isotropic Radiated Power (EIRP) values have been assumed for main and side lobes as derived by the European Space Operations Center (ESOC) to enable preliminary scientific investigations in support of the PROBA-3 mission [10].

It consists in an oversimplified stair steps pattern, represented in Figure 3.9, that approximates the average behaviour of the Galileo constellation, albeit it will lead to sharp variations in the satellite visibility.

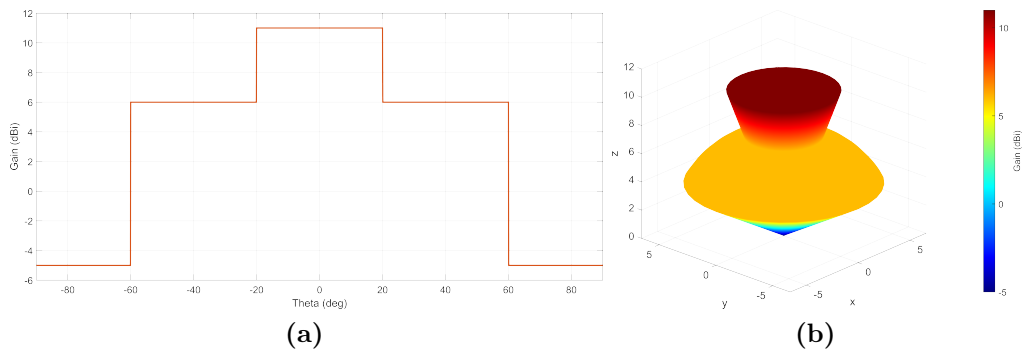


Figure 3.9: Galileo ESA/ESOC model antenna pattern 2D (a) and 3D (b) representation. Constant for every azimuthal angle.

3.3.3 Geometric and Radiometric visibility

Given a satellite and the receiver states, two types of visibility are defined:

- **Geometric visibility:** is a measure of the instantaneous availability of a direct Line-Of-Sight (LOS) between the spacecraft and the satellite vehicle antenna pattern, for which a 90° off-boresight angle mask is adopted. If so, then the satellite can be considered *geometrically visible*. It can be negatively impacted when the satellite-spacecraft baseline exceeds an off-boresight angle of 90 degrees from the nadir pointing direction, or as a result of occultation effects that occur due to the presence of the Earth or the Moon, as illustrated in Figure 3.10.

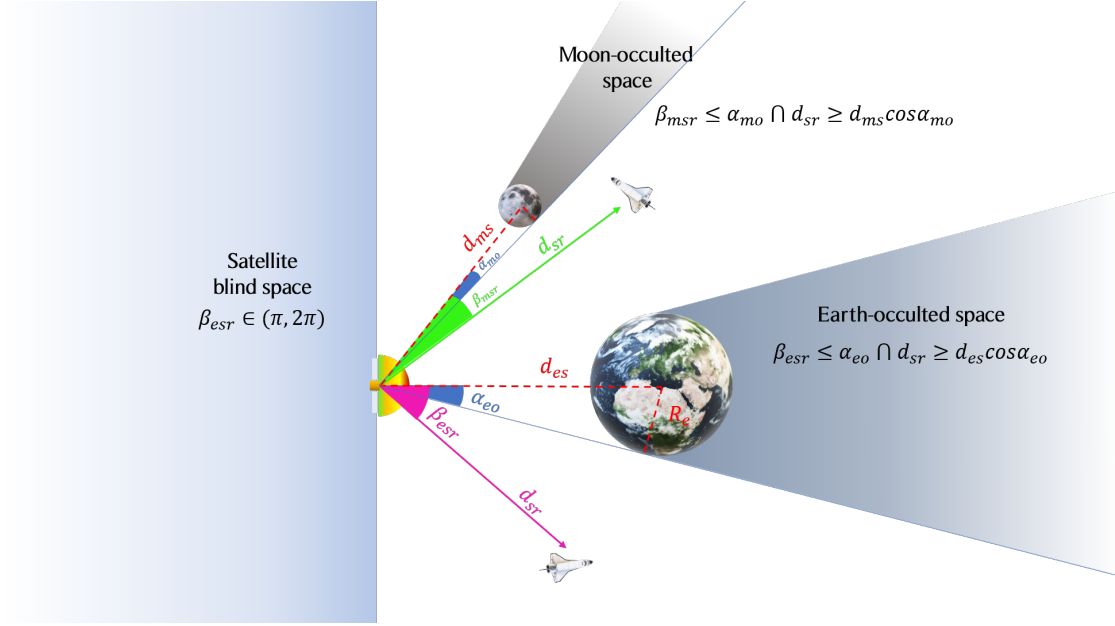


Figure 3.10: SV geometric visibility example with Earth occultation angles and distances.

Two *occultation angles* are defined for Earth and Moon:

$$\alpha_e = \arctan(R_E/d_{es}) \quad (3.14)$$

$$\alpha_m = \arctan(R_{moon}/d_{ms}) \quad (3.15)$$

where d_{es} and d_{ms} are the distances of Earth and Moon from the station vehicle.

$$d_{es} = \sqrt{(x_e - x_{sv})^2 + (y_e - y_{sv})^2 + (z_e - z_{sv})^2} \quad (3.16)$$

$$d_{ms} = \sqrt{(x_m - x_{sv})^2 + (y_m - y_{sv})^2 + (z_m - z_{sv})^2} \quad (3.17)$$

Earth occultation occurs when the angle Earth-SV-Receiver β_{esr} is smaller than α_e and the Receiver is not between Earth and the satellite (under the Terrestrial Service Volume (TSV)).

$$\beta_{esr} \leq \alpha_{eo} \cap d_{sr} \geq d_{es} \cos \alpha_{eo} \quad (3.18)$$

Similarly, there is Moon occultation when the Moon stands between the receiver and the satellite, and the angle Moon-Receiver-SV β_{mrs} is smaller than α_m .

$$\beta_{msr} \leq \alpha_{mo} \cap d_{sr} \geq d_{ms} \cos \alpha_{mo} \quad (3.19)$$

where d_{sr} is the Euclidean distance between the satellite and the receiver.

- **Radiometric visibility:** depends on the received signal-to-noise ratio associated with the selected satellite. In particular, for a passband signal, we usually refer to the Carrier-to-Noise power density Ratio (CNR or C/N_0) [11]. If it is above a certain threshold, then the satellite can be considered radiometrically visible or RF-visible. Note that geometric visibility is a necessary but not sufficient condition for radiometric visibility to occur.

The link budget for the C/N_0 of a communication link between the receiver and a given satellite is defined as in [1].

$$C/N_0 = P_T + G_T(\phi, \theta) - 20 \log\left(\frac{4\pi d}{\lambda_{L1}}\right) - G_R(\phi, \theta) - L_{pol} - 10 \log(kT_{sys}) - R_{loss} \quad (3.20)$$

where the parameters included in Table 3.4 were considered.

Receive Side		Transmit Side	
Parameter	Value	Parameter	Value
System Implementation Losses (R_{loss})	0.9 dB	GPS Block IIR (P_T)	17.3 dBW
System Temperature (T_{sys})	162 K	GPS Block IIR-M (P_T)	18.8 dBW
Polarization Losses (L_{pol})	1 dB	GPS Block IIF (P_T)	16.2 dBW
Receive Antenna Gain ($G_R(peak)$)	16 dB	Galileo ($P_T + G_T(peak)$)	11 dBW

Table 3.4: Link budget parameters.

Figure 3.11 shows a realization sample of the framework. The program generates a scenario for all GPS and Galileo satellites based on a given date and the spacecraft’s position. Moreover, it identifies the RF-visible satellites by highlighting their antenna patterns, given a Radiometric visibility threshold. For each satellite, a set of arrows pointing towards the sun and towards the spacecraft can optionally be shown.

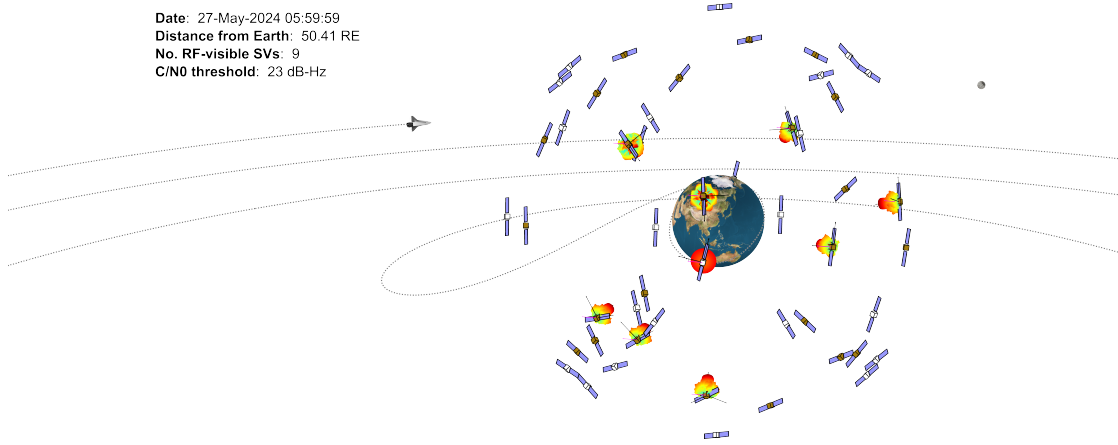


Figure 3.11: Simulation framework example.
Satellites showing their antenna patterns are RF-visible.

3.4 Observables generation

In the case of radiometric visibility, the receiver can “measure” the observables from the radionavigation signal. In practice, for this framework, the observables are simulated with noise to form the measurements the receiver would get as input to the navigation filter.

Pseudorange

The *Pseudorange* is defined as the difference between the time of reception (expressed in the time frame of the receiver) and the time of transmission (expressed in the time frame of the satellite) of a distinct satellite signal, expressed in meters. This corresponds to the distance from the receiver antenna to the satellite antenna, including receiver and satellite clock offsets and other biases, such as atmospheric delays.

For a signal from the satellite (s), the pseudorange $P_r^{(s)}$ can be expressed by using the signal reception time $t_{rx}^{(s)}|_r$ measured by the receiver clock and the signal transmission time $t_{tx}^{(s)}|_s$ measured by the satellite clock as:

$$P_r^{(s)} = c(t_{rx}^{(s)}|_r - t_{tx}^{(s)}|_s) \quad (3.21)$$

where:

$$t_{rx}^{(s)}|_r = t_{rx}^{(s)} + \Delta t_r \quad (3.22)$$

$$t_{tx}^{(s)}|_s = t_{tx}^{(s)} + \Delta t_s \quad (3.23)$$

More specifically, not only does the pseudorange equation have to consider the geometric range $\rho_r^{(s)}$ between satellite and receiver antennas, namely their mutual geometric distance, but it has also to take into account the receiver and satellite clock biases Δt_r and Δt_s with respect to the common Universal Time Coordinated (UTC) reference time, the ionospheric and tropospheric delays $I_r^{(s)}$ and $T_r^{(s)}$ and the measurement error ϵ_P .

$$\begin{aligned} P_r^{(s)} &= c[(t_{rx}^{(s)} + \Delta t_r) - (t_{tx}^{(s)} + \Delta t_s)] + I_r^{(s)} + T_r^{(s)} + \epsilon_P \\ &= c(t_{rx}^{(s)} - t_{tx}^{(s)}) + c(\Delta t_r - \Delta t_s) + I_r^{(s)} + T_r^{(s)} + \epsilon_P \\ &= \rho_r^{(s)} + c(\Delta t_r - \Delta t_s) + I_r^{(s)} + T_r^{(s)} + \epsilon_P \end{aligned} \quad (3.24)$$

Although the signals coming from geometrically visible satellites might cross a significant portion of the atmosphere, the framework neglects the errors due to Ionosphere $I_r^{(s)}$ and Troposphere $T_r^{(s)}$, as an implementation choice to simplify the modelling of the system and because they are not significant for the study carried out in the thesis. Moreover, the bias term due to the satellite clock offset is assumed to be corrected, as it can be usually done from GPS/Galileo base station information.

Therefore the pseudorange measurement is simply generated as:

$$P_r^{(s)} = \rho_r^{(s)} + c\Delta t_r + \epsilon_P \quad (3.25)$$

The term $c\Delta t_r$ is the receiver clock bias, expressed in meters, which is simulated according to Equation (3.12), whereas ϵ_P is the pseudorange measurement noise modelled by Fig. 3.12a.

Pseudorange rate

The *Pseudorange rate*, as mentioned in the previous chapter, can be considered as the projection of the relative velocity vector on the direction from the receiver to the satellite:

$$\Delta P_r^{(s)} = (\mathbf{v}_s - \mathbf{v}_r) \cdot \frac{\mathbf{r}_s - \mathbf{r}_r}{|\mathbf{r}_s - \mathbf{r}_r|} \quad (3.26)$$

Doppler shift

From Equation (2.14), the *Doppler shift* is obtained as:

$$f_D = -\frac{f_{L1}}{c} \Delta P_r^{(s)} \quad (3.27)$$

To obtain the Doppler shift measurement, Equation (3.27) has still to be noise-stained with a white noise modelled by Fig. 3.12b.

Doppler rate

The *Doppler rate* is simply simulated as the time derivative of the Doppler shift:

$$\frac{\partial f_D}{\partial t} = \Delta f_D^k = \frac{f_D^k - f_D^{k-1}}{t_k - t_{k-1}} \quad (3.28)$$

3.4.1 Measurement noise

Similarly to what is done in LuGRE analysis [1], measurement noise is modelled as a function of the received C/N0, which is applied as White Gaussian Noise (WGN). In particular, the standard deviation of the noise is modelled according to the curves presented in the paper and visually reconstructed.

Starting from a general parametric exponential function (Eq. 3.29), the noise standard deviation models for the pseudorange (Fig. 3.12a) and the Doppler shift (Fig. 3.12b) have been reconstructed according to the parameters reported in Table 3.5 to best resemble the curves presented in [1].

$$f(x) = a \cdot b^{(x-x_0)} + c \quad (3.29)$$

1σ noise model	<i>a</i>	<i>b</i>	<i>c</i>	<i>x</i> ₀
Pseudorange	26.7000	1.125	0	15
Doppler Shift	0.0325	1.350	0.0125	15

Table 3.5: 1- σ noise model parameters.

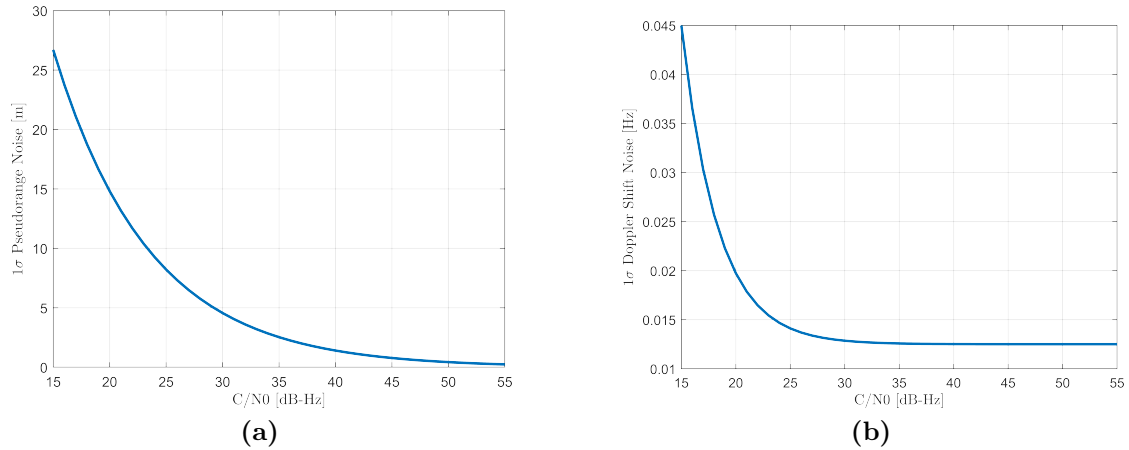


Figure 3.12: 1- σ noise model for Pseudorange (a) and Doppler shift (b) measurement noise.

As explained in [1], the constant offset in the Doppler noise model, represents the proportion of the total noise due to the clock instability, where the clock is assumed to be modelled similarly to the one of this simulation framework.

3.5 Navigation filters

The generated observables are then ready to be processed by one of the three different navigation filters to simulate the position estimation:

- **Least Mean Square filter**
- **Extended Kalman Filter**
- **Trajectory-Aware Extended Kalman Filter**

The generated measurements are input into these filters, and the PVT solution is computed.

Note that EKF and TA-EKF need to be initialized, therefore the LMS filter is used to make a first position estimate for the first ten epochs. This estimate is then used in Kalman filters which are expected to give better performances than the LMS. Furthermore, some filter matrices may need fine-tuning of their parameters to get optimal performances, and this tuning might change depending on the geometry of the problem.

The LMS filter is configured with a number of iterations equal to 20, so to have a reliably precise estimation. Please, notice that the LMS filter is used only as a first

reference, therefore its analysis was not thorough. To make a fairer comparison, as a first enhancement, a Weighted Least Mean Square (WLMS) could be used, where the weighted matrix depends on the signal strength, as the Observation noise covariance matrix does in the Kalman filters. Then a memory of the last state could be introduced in the system to help the convergence and improve the accuracy.

As for the Kalman filters, they both were initialized through the LMS filter. In particular, a “conservative” amount of ten LMS solutions is considered for the first ten epochs, but it can be decreased at will, letting Kalman filter work since the second epoch. Coming to the KF architecture, the state noise covariance matrix Q , is defined as in 2.46 where the acceleration noise power spectral density S_p is set to $50 \text{ m}^2/\text{s}^3$ for the plain Extended Kalman Filter (EKF) and $2 \text{ m}^2/\text{s}^3$ for the Trajectory-Aware Extended Kalman Filter (TA-EKF).

As for the state error covariance matrix P , it is initialized assuming an independent uncertainty of 10 meters per dimension, which converted to covariance matrix became:

$$P = \begin{bmatrix} 100 & 0 & 0 & 0 & 0 & 0 & 0 & 0 \\ 0 & 100 & 0 & 0 & 0 & 0 & 0 & 0 \\ 0 & 0 & 100 & 0 & 0 & 0 & 0 & 0 \\ 0 & 0 & 0 & 100 & 0 & 0 & 0 & 0 \\ 0 & 0 & 0 & 0 & 200 & 0 & 0 & 0 \\ 0 & 0 & 0 & 0 & 0 & 200 & 0 & 0 \\ 0 & 0 & 0 & 0 & 0 & 0 & 200 & 0 \\ 0 & 0 & 0 & 0 & 0 & 0 & 0 & 200 \end{bmatrix} \quad (3.30)$$

Notice that a doubled uncertainty characterizes the velocity components of the state as they result from a difference between two random variables.

Finally, the observation noise covariance matrix R is defined by weighting the measurements by their associated received power. In particular, the following model was adopted:

$$R = I_{2N} \circ (ru^T) \quad (3.31)$$

The operator (\circ) represents the Hadamard product used to define R as a diagonal matrix.

In particular:

- N is the number of RF-visible satellites
- I_{2N} is the identity matrix of size $2N \times 2N$
- $u = [1, \dots, 1]$ of size $1 \times 2N$

- $r = \{r_i\}$ of size $1 \times 2N$

Equation 3.32 describes the models used for the noise variance of satellite pseudorange ($1 \leq i \leq N$) and pseudorange rate ($N + 1 \leq i \leq 2N$), according to the general model, presented in [12], and with parameters adapted to the space context.

$$r_i = \begin{cases} 1 + 281^2 \cdot 10^{-\frac{C/N_0}{10}}, & \text{if } i \leq N \\ 10^{-4} + 5^2 \cdot 10^{-\frac{C/N_0}{10}}, & \text{otherwise} \end{cases} \quad (3.32)$$

The TA-EKF requires a matching strategy to identify the corresponding state to the last PVT estimate in the expected orbital trajectory used for assistance. This process can be difficult due to various factors affecting the matching algorithm. However, in our specific scenario, the aiding trajectory is identical to the ground-truth trajectory, meaning that there is a straightforward one-to-one correspondence between the trajectory samples and PVT estimates.

In general, the aiding trajectory differs from the ground-truth trajectory, although it is expected to closely resemble it. Therefore, the framework assumes no knowledge of the aiding trajectory. At each epoch k , the framework selects the expected trajectory state for the k -th epoch (\mathbf{x}_k^*) as a starting point to locate the corresponding aiding state for the next filter iteration. The corresponding aiding state ($\tilde{\mathbf{x}}_k$) is then determined by calculating the average of its surrounding states.

Given a radius r :

$$\tilde{\mathbf{x}}_k = E\{\mathbf{x}_i^*\}, \quad \forall i \in \{k - r, k - r + 1, \dots, k + r\} \quad (3.33)$$

A radius of four samples has been selected arbitrarily for this orbital trajectory.

Chapter 4

Simulation results

The outcomes obtained through the employment of the simulation framework previously illustrated are presented in this chapter. Firstly, the reliability of the simulation tool is scrutinized to lend support to the performance comparison of the distinct algorithms that require testing. Following that, an extensive evaluation of the simulation scenario is conducted to attain a comprehensive understanding of the positioning problem and forecast the anticipated performances of the diverse algorithms. Finally, in the contest of LuGRE mission, an in-depth examination of a mission point is carried out using a highly precise and dependable Montecarlo simulation, and the final results are extrapolated to compare the various navigation filters.

4.1 Mission overview

The mission is characterized by a realistic Earth-Moon Transfer Orbit (MTO), expressed according to the ECEF reference frame. Its features are represented in terms of distance from Earth in Figure 4.1a and of x,y and z components of the vehicle velocity in Figure 4.1b).

As illustrated in the figures, the spacecraft trajectory is characterized by three *phasing loops*. Phasing loops are a series of manoeuvres that a spacecraft performs to adjust its trajectory and match the orbit of another celestial body, such as the Moon ([13],[14] and [15]). These manoeuvres are critical for spacecraft that are travelling to the Moon because they allow the spacecraft to time its arrival at the Moon so that it can enter into orbit around it.

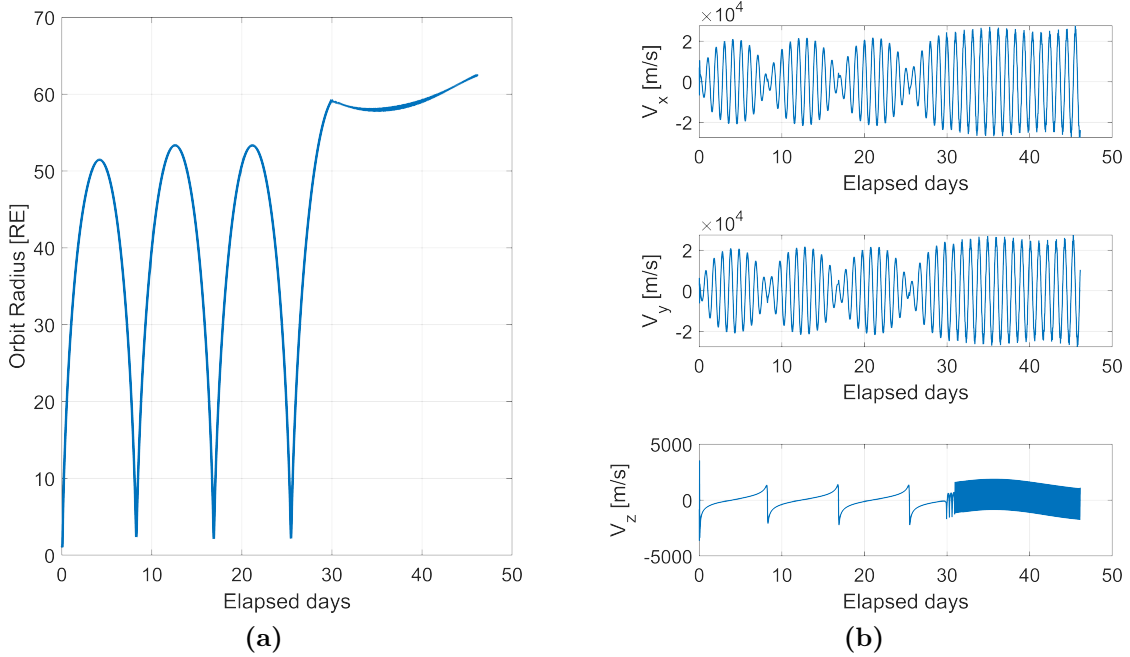


Figure 4.1: Mission Orbit Radius (a) and Velocity (b) as function of elapsed time.

The phasing loops technique involves using the gravitational pull of the Moon to adjust the spacecraft's trajectory. The spacecraft will perform a series of small engine burns at strategic points in its trajectory, which will adjust its speed and direction. By carefully timing these burns, the spacecraft can use the Moon's gravity to "slingshot" it into the correct orbit. The spacecraft typically follows a trajectory that takes it around the Earth and then out toward the Moon. As the spacecraft approaches the Moon, it will perform a series of engine burns to adjust its speed and direction. These burns will gradually adjust the spacecraft's trajectory until it matches the Moon's orbit. Once the spacecraft is in the correct position, it can perform a final engine burn to enter into orbit around the Moon.

Phasing loops are a common technique used by spacecraft travelling to the Moon because they are an efficient way to adjust the spacecraft's trajectory using minimal fuel. They require careful planning and execution, but they are critical for ensuring that the spacecraft arrives at the Moon at the right time and in the right orbit.

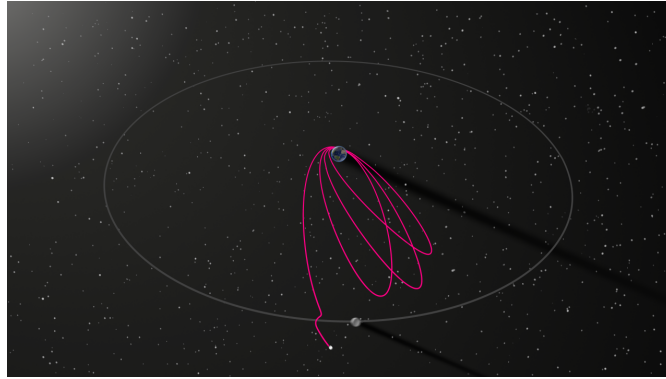


Figure 4.2: NASA’s Wilkinson Microwave Anisotropy Probe (WMAP) phasing loops. WMAP orbits around Earth waiting for the moon to move into the right position. This is about a three week process.

Consequently, Doppler shift and Doppler rate are generated along the mission. For example, for satellite GPS SVN56, the measurements follow the trends shown in Figures 4.3a and 4.3b. In general, a GNSS Station Vehicle (SV) is not seamlessly visible, therefore its associated quantities are exploited only in the case of radiometric visibility.

Notice that Doppler measurements strongly relate to the relative speed of the SV with respect to the receiver. A clear example of this can be observed by comparing the Doppler rate 4.3b with the receiver velocity 4.1b: an abrupt acceleration of the receiver corresponds to a sharp variation in the Doppler frequency.

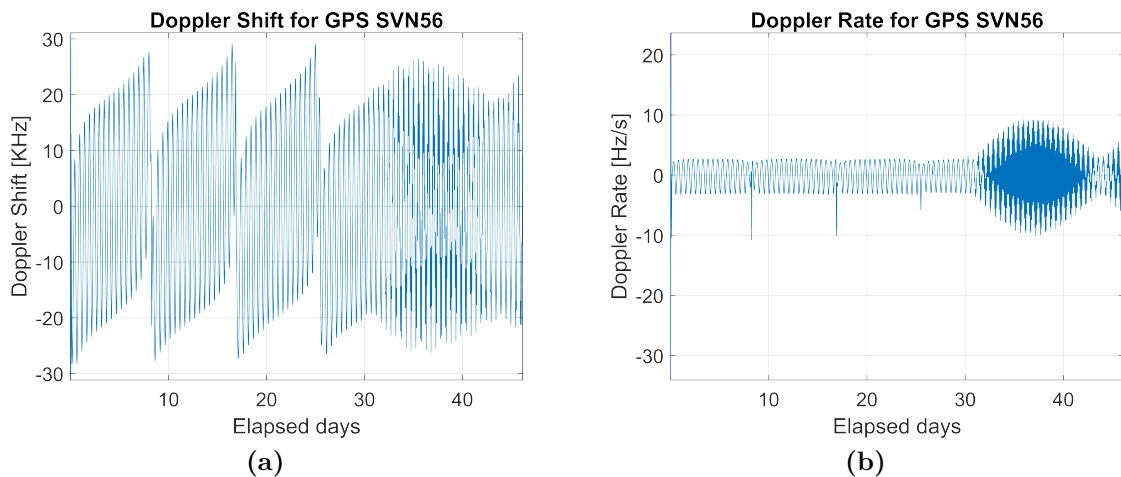


Figure 4.3: Doppler shift (a) and Doppler rate (b) for GPS station vehicle SVN56 as function of the mission elapsed time.

4.1.1 GNSS satellite distribution

GPS and Galileo station vehicles are simulated according to their expected orbit progression, and their geometry is analyzed for the PVT evaluation.

Radiometric visibility

Figures 4.4a, 4.4b, 4.5a and 4.5b depict the expected GPS-only, Galileo-only, and combined GPS/Galileo radiometric visibility throughout the elliptical phasing orbits and low lunar orbits of the transit phase as a function of distance from the Earth (a) and of mission time (b). In these figures, the dots represent the number of RF-visible GNSS satellites every 15 minutes throughout the trajectory, while the triangles represent a moving average of the number of RF-visible GNSS satellites.

On average, Galileo shows a lower availability in MTOs mainly due to its lower transmit power with respect to GPS satellites (Table 3.4). Moreover, the Galileo satellite visibility trend presents a sharp drop-off in the number of visible satellites due to the conservatism of the Galileo EIRP pattern discussed in 3.3.2.

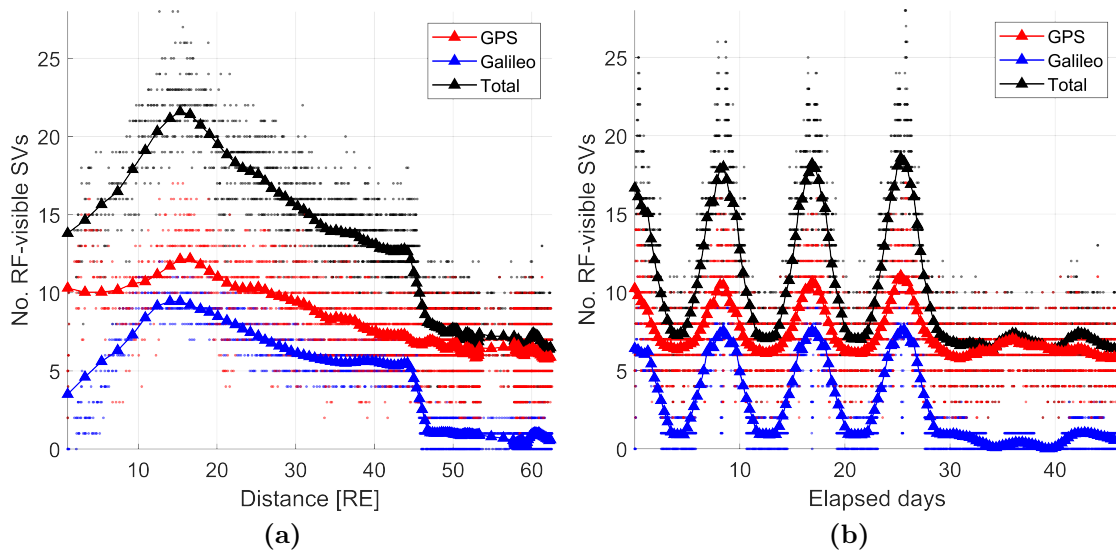


Figure 4.4: Radiometric visibility ($C/N_0 \geq 20$ dB – Hz) as function of mission distance (a) and elapsed time (b).

Beyond the mean expected visibility, fewer or more satellites may be intermittently visible. For example, at 50 RE altitude, 6 GNSS satellites are visible on average when using a 23 dB-Hz threshold (Fig. 4.5a), but that instantaneous number may be as high as 11 or as low as 0.

Figures 4.4a and 4.4b show visibility trends for an assumed nominal C/N_0

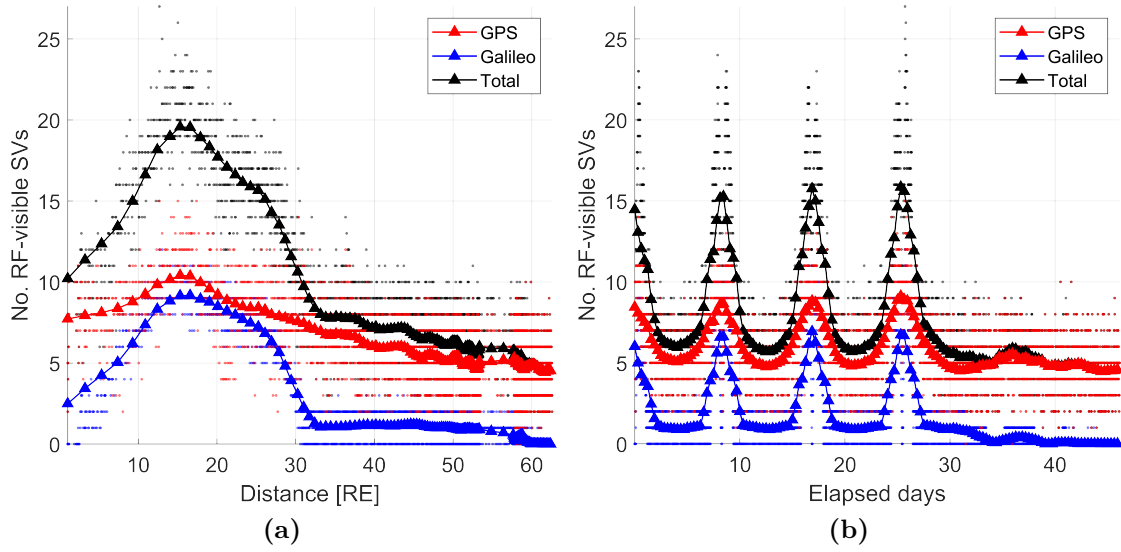


Figure 4.5: Radiometric visibility ($C/N_0 \geq 23$ dB – Hz) as function of mission distance (a) and elapsed time (b).

threshold of 20 dB-Hz, while Figures 4.5a and 4.5b show the same trend for an assumed C/N_0 threshold of 23 dB-Hz to account for a 3 dB link margin. It is expected that the actual visibility observed during the flight is likely to fall within the range represented by these two sets of information, being the declared receiver sensitivity of 20 dB-Hz. The primary difference between the two thresholds is that a higher threshold removes an average of 1-2 satellites, with a much earlier drop-off in Galileo visibility (at 45 RE vs. at 30 RE, respectively).

These results are in line with those obtained in [1], so it can be assumed that the assumptions made in the simulation environment are valid to exploit the simulation environment for obtaining significant analysis.

Geometric arrangement

The geometric arrangement of the satellites is crucial for an accurate solution to the PVT problem and it can be analyzed by looking at the GDOP which reflects the impact of the geometry in position estimation accuracy (Figs. 4.6a and 4.6b).

As expected, the farther the spacecraft with respect to the Earth, the worse the GDOP. This is immediate to see if you think that when you are close to the Earth, you need to have a large angle of view to visualize all RF-visible satellites; on the contrary, when you are far from Earth, whatever satellites are distributed, they will always be concentrated in a tight angle of view. Therefore, GDOP typically has a value that increases with distance.

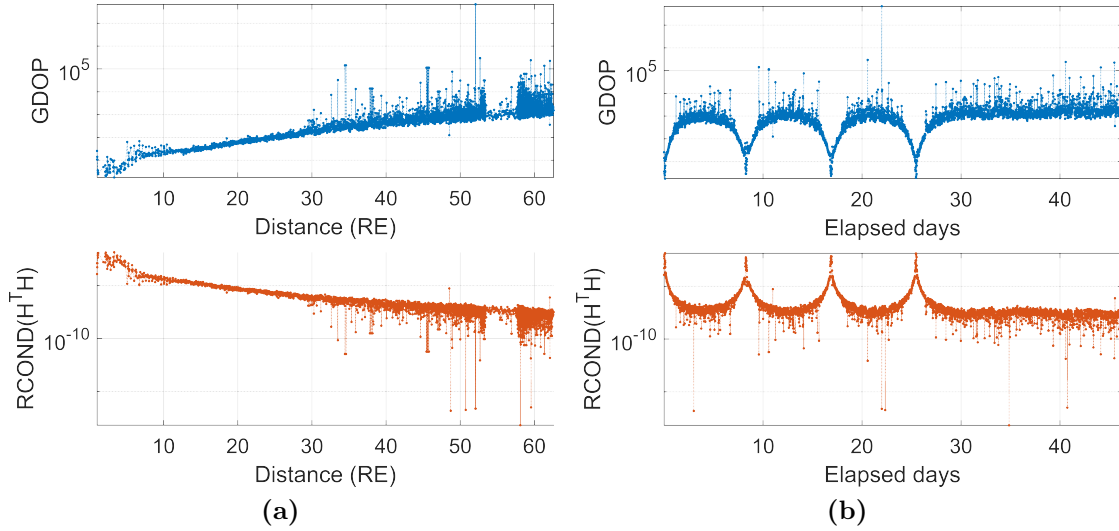


Figure 4.6: Least Square GDOP and reciprocal condition of Gramian matrix as function of mission distance (a) and elapsed time (b).

4.1.2 Expected GNSS performances

The GDOP behaviour allows us to foresee what positioning performances to expect, given the standard deviation of the positioning error defined by 1.20.

Figure 4.7 qualitatively represents how the error is expected to increase for a PVT EKF solution, the farther the spaceship gets from the Earth.

In particular, the position estimation uncertainty out of the EKF is depicted through an error covariance ellipsoid generated every time a position estimation is carried out, that is for this example, every 15 minutes. It is centred on the estimated position and is characterized by three axes a , b and c generated starting from the position estimation error covariance matrix. Its eigenvectors define the main directions of the 3-dimensional error ellipsoid and the eigenvalues are the squares of the semi-axes [16].

For the Kalman Filters (KFs), the error covariance matrix is given as an outcome. Albeit it is defined as an 8×8 matrix, a 3×3 sub-matrix corresponding to the position states can be considered.

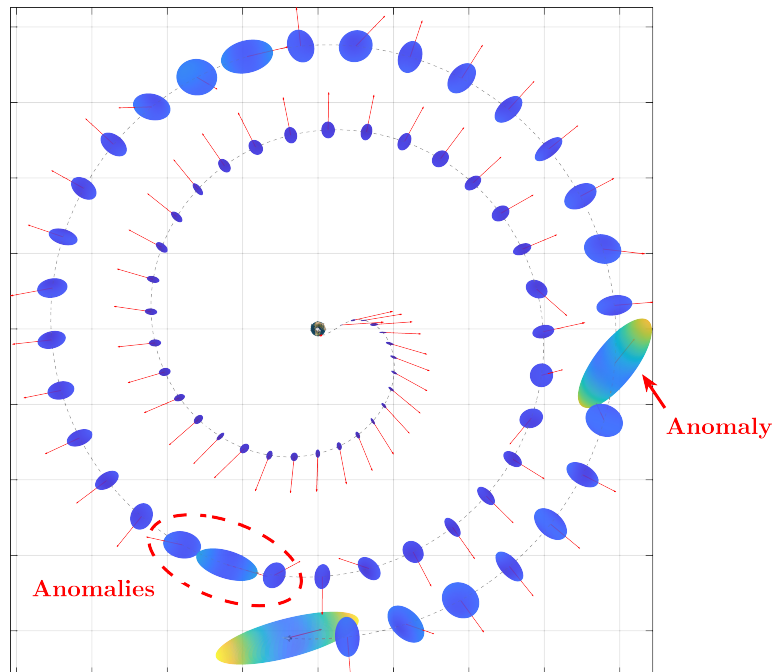


Figure 4.7: Error covariance ellipsoids from EKF results and covariance anomalies due to bad geometry.

This representation highlights how geometry affects positioning uncertainty. A general increasing trend can be observed for the ellipsoid sizes the larger the distance from Earth. Furthermore, a peculiarity of the GNSS geometric problem is pointed out: major uncertainties mainly affect the direction which the signals come from. However, there can occur cases in which other directions are affected by very large uncertainties as well: we will refer to these epochs as “covariance anomalies” or, simply, “anomalies”.

The cause of covariance anomalies can be found both in the distribution of the satellites, in terms of GDOP and visibility, and in the dynamics of the receiver. From Figure 4.8, it can be seen that the largest anomalies correspond to the points in which the GDOP has a sudden variation towards greater values, i.e. the points in which the geometry of the problem suddenly gets much worse. Furthermore, the size of the ellipsoids also depends on the number of RF-visible satellites. Clearly, the larger the distance from Earth, the fewer satellites are visible and the higher the likelihood of a bad satellite geometric distribution leading to high GDOP and increasing as a consequence the estimation uncertainty.

However, there is no unequivocal link between the two conditions, particularly thanks to the use of Kalman Filters. Indeed, Kalman filters include further

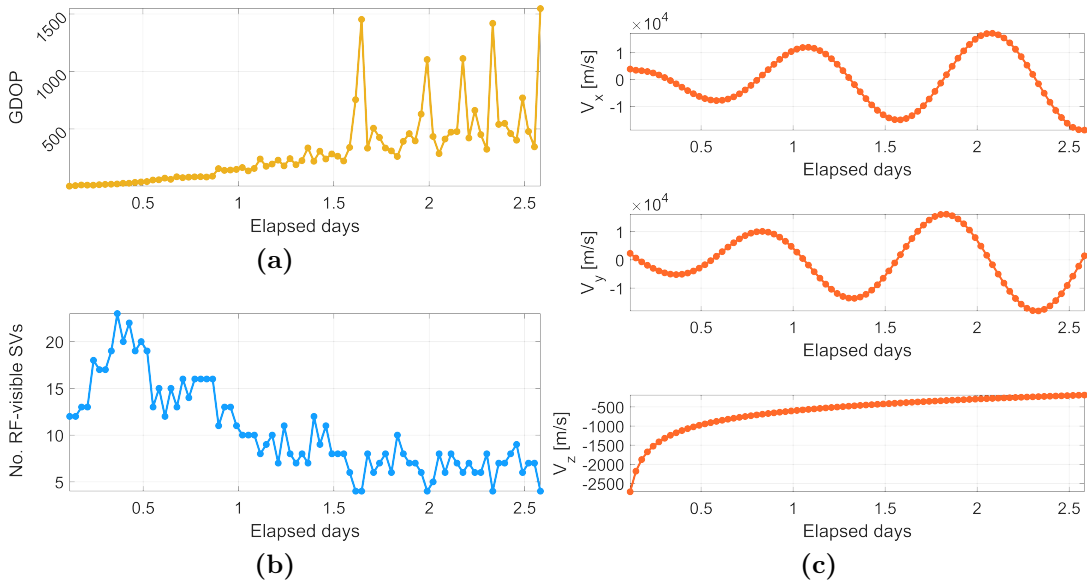


Figure 4.8: GDOP (a), Satellite Visibility (b) and Receiver Dynamics (c) at covariance ellipsoid epochs.

information like the system dynamics and the expected trajectory. In light of this, other minor anomalies may occur when the dynamics of the receiver are characterized by nonlinearities not well described by the linear model used in the KFs.

4.2 Case study: LuGRE planned mission period

In order to evaluate the effectiveness of the proposed TA-EKF architecture, a specific portion of the mission trajectory was identified that is relevant to the scientific objectives of the mission. Notice that a 3 dB link margin is considered for Radiometric visibility, which is assumed verified with a CNR above 23 dB-Hz.

The planning schedule of payload operations for LuGRE [17] is taken as reference. Figure 4.9 depicts the plan in distance from the Earth. Yellow circles represent the location of manoeuvres, whereas brown dots represent a baseline set of 15 planned 1-hour periods where LuGRE will be oriented to the Earth for data collection.

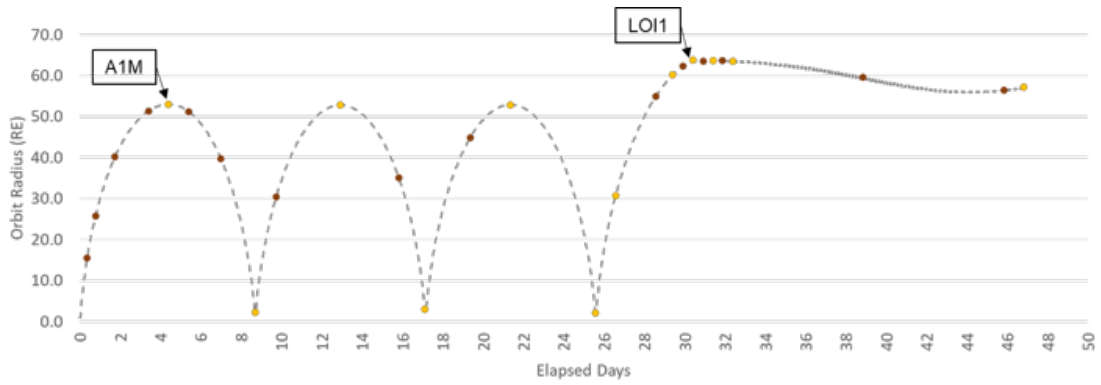


Figure 4.9: LuGRE Operations Schedule During Transit.

In particular, the second planned mission point is selected within a 2-hour neighbourhood (Fig. 4.10) to better analyze filters convergence.

Particular attention is paid to a segment where the y -component of the velocity exhibits a slight nonlinearity, shown in Figure 4.10, which is anticipated to slightly negatively impact the algorithm outcome.

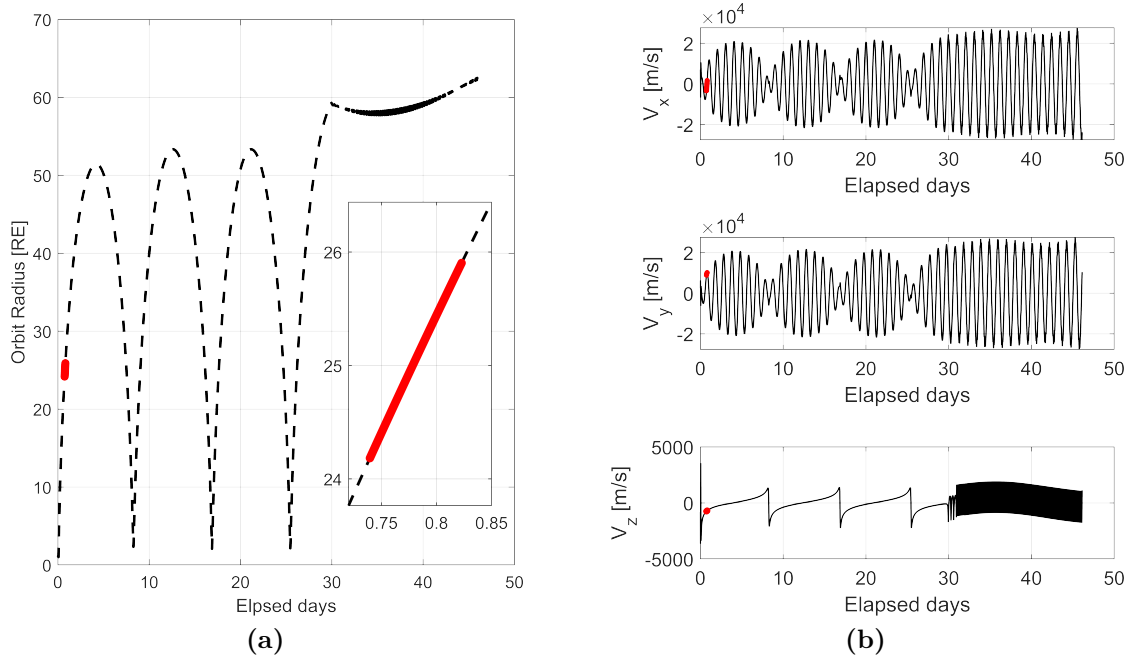


Figure 4.10: Mission point 2: Orbit Radius (a) and Velocity (b) as function of mission elapsed time.

Simulation results

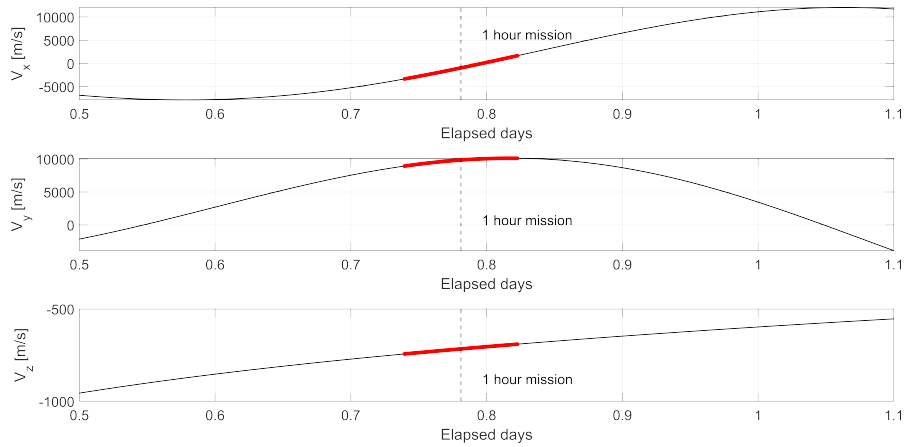


Figure 4.11: Mission segment analyzed velocity states.

A pictorial overview of the analyzed mission segment is provided in Figure 4.12, and the system state is represented in terms of visibility and geometric arrangement quality in Figures 4.13 and 4.14, respectively. It can be deduced that this mission point is quite favourable to GNSS receivers to work with acceptable performances.

Finally, observables, such as pseudorange and Doppler measurements, are simulated according to the models described in the previous chapter for the current mission segment. Figure 4.15 shows an example of Doppler measurements with respect to the GPS satellite SVN56.

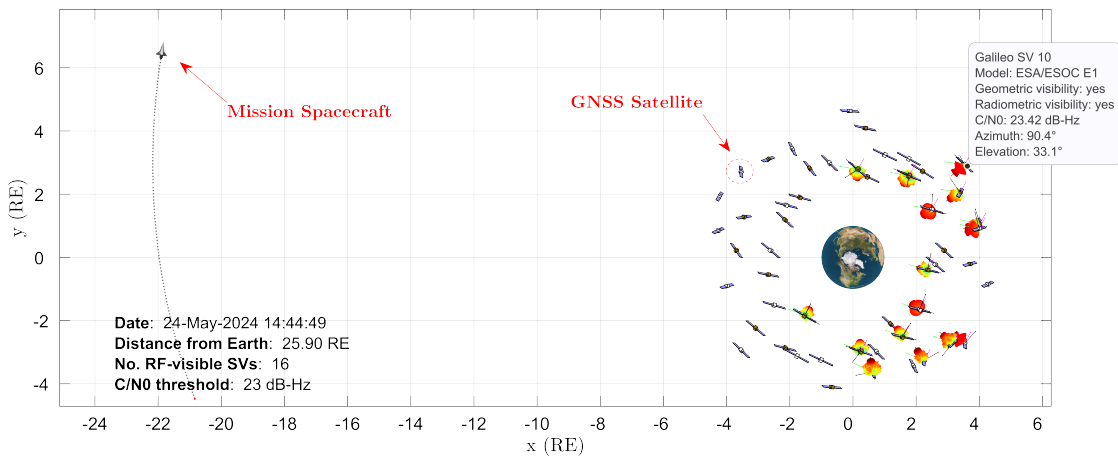


Figure 4.12: Mission segment framework realization.

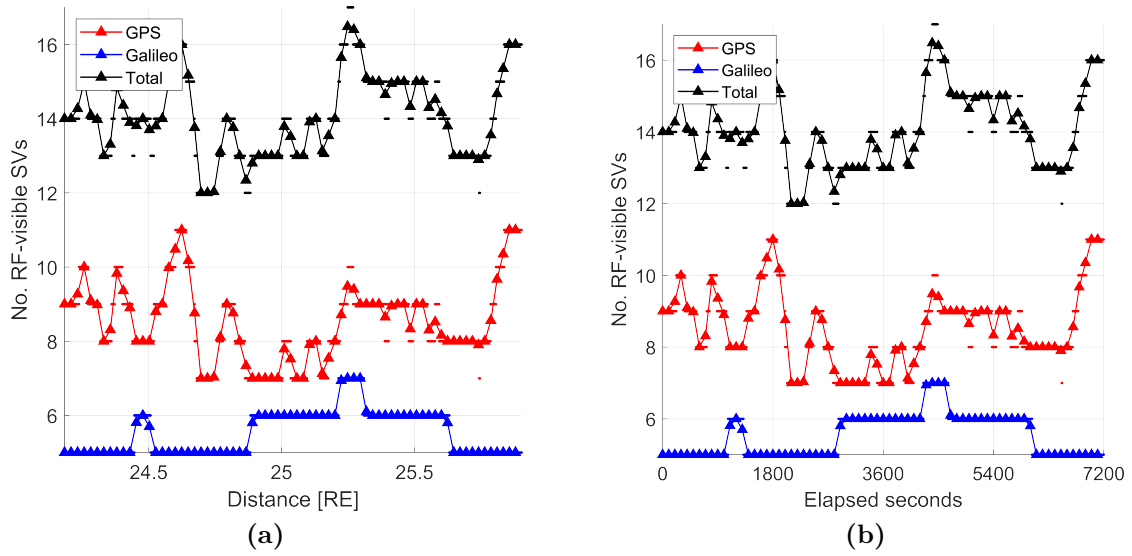


Figure 4.13: Mission segment satellite Radiometric visibility ($C/N_0 \geq 23$ dB – Hz) as function of mission distance (a) and elapsed time (b).

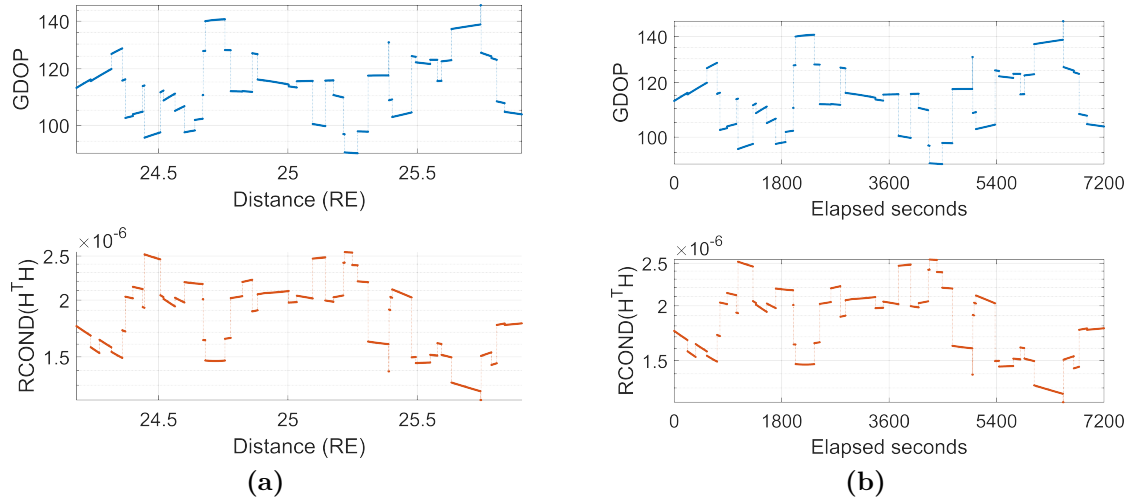


Figure 4.14: Least Square GDOP and reciprocal condition of Gramian matrix as function of the mission segment distance (a) and elapsed time (b).

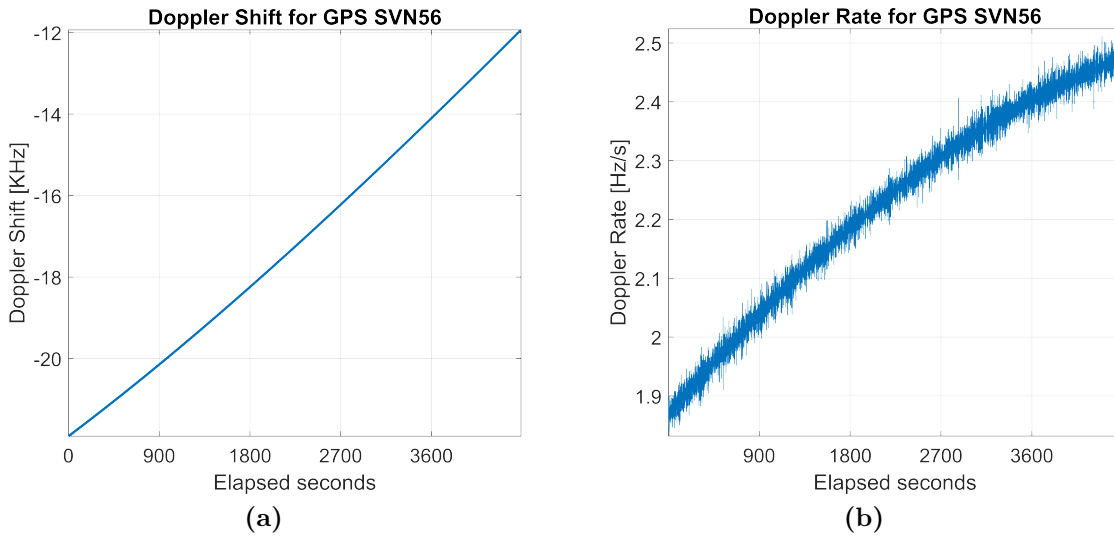


Figure 4.15: Doppler shift (a) and Doppler rate (b) for GPS station vehicle SVN56 as function of the mission segment elapsed time. Note that the station vehicle SVN56 gets out of radiometric visibility after 4490 seconds since the mission segment started.

4.2.1 Navigation filters comparison

To make a more statistical description of the outcomes, the results come from a series of Monte Carlo simulations. For timing reasons, the test could not run many simulations, therefore 100 Monte Carlo realizations have been carried out. Although they are not sufficient to statistically evaluate the proposed solution, they show interesting results that should be furtherly examined.

The navigation filter performances are expressed in terms of the experimental cumulative distribution function of the positioning error.

As can be observed from the following figures, the Least-Mean-Squares (LMS) solution can not guarantee good performance in space applications, mainly because of the bad geometry that Navigation Systems provide in such contexts.

Standard EKF allows an increment in precision, that can be further enhanced with the aided version proposed in this work (the TA-EKF), gaining a total of almost one order of magnitude in accuracy.

The global comparison of the three filters under test is represented in Figure 4.16a.

In particular, the focus is on the difference between the standalone EKF and the custom Trajectory-Aware version.

Table 4.1 provides a summary of the cumulative statistics at various percentiles as illustrated in Figure 4.16b. The accuracy of the TA-EKF architecture is significantly

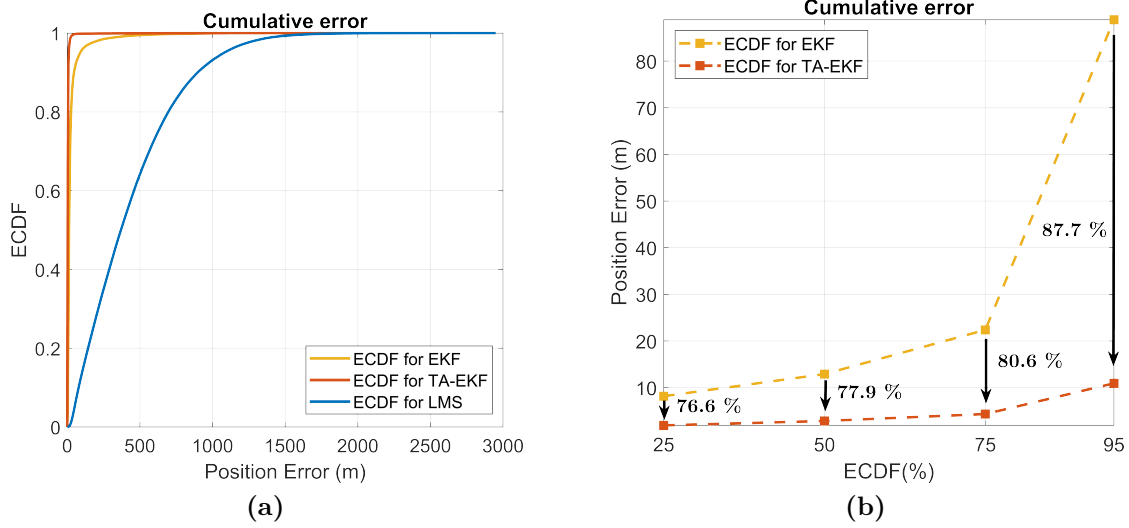


Figure 4.16: Empirical Cumulative Distribution Function (ECDF) for the positioning error in ECEF-coordinates for LMS, plain EKF and TA-EKF filters (a) and cumulative error comparison for EKF and TA-EKF (b).

better than that of a plain EKF. For example, at the 95th percentile, the accuracy improvement reaches 87.7%. This is due to the introduction of aiding information, such as the expected MTO trajectory, which enables the navigation filter to counteract the degrading effects of the poor geometry conditions experienced during the MTO. These results were obtained despite the use of a simplified model to characterize the process dynamics between discrete-time filter iterations.

Navigation Filter	Error Percentile (m)			
	25th	50th	75th	95th
Plain EKF	8.16	12.91	22.38	88.88
TA-EKF	1.91	2.85	4.34	10.93

Table 4.1: Positioning error for plain EKF and TA-EKF considering 7200 epochs at 1 Hz.

Concerning the Kalman filter Error Covariance Matrix (ECM) convergence, the two filters have similar performances. The following figures show the behaviour of the A-Posteriori ECM in terms of position, velocity, bias and drift error.

The high dynamics of the spacecraft require the adoption of a constant velocity approximation (i.e., high acceleration noise), which affects the process state estimate

and covariance estimate. However, the introduction of an aiding state in the proposed TA-EKF improves model linearization and leads to enhanced state estimates. Consequently, the convergence pattern of estimation error covariance statistics (Fig. 4.17) improves, namely, the estimation uncertainty decreases.

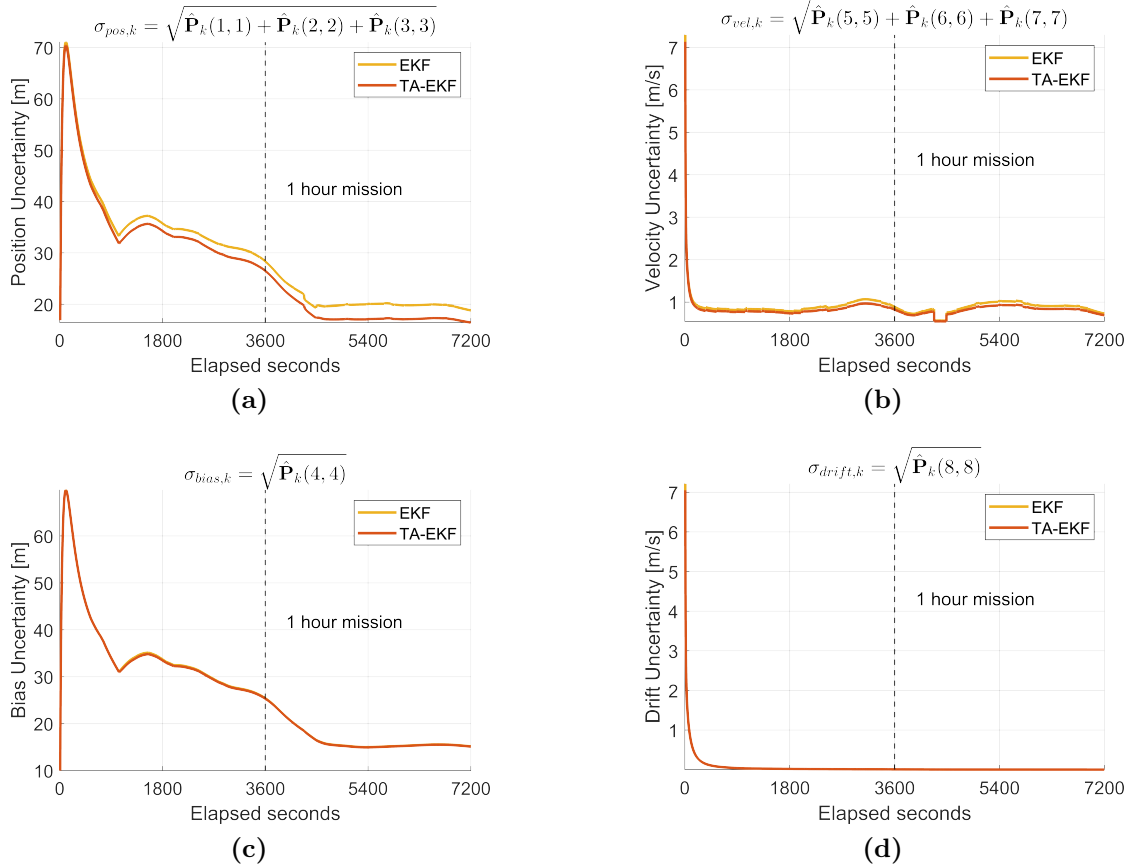


Figure 4.17: Time-series of the 1σ -dispersion of the navigation filter estimates for the Position (a), Velocity (b), Clock Bias (c) and Clock Drift (d) states. Comparison between plain EKF and TA-EKF.

Consequently, the two Kalman filters show similar trends also for the error covariance ellipsoids. Figure 4.18 depicts the error covariance ellipsoids generated for the Kalman filters in the analyzed mission segment. Observations similar to the general case can be made.

However, it is worth noting that even with slight nonlinearities in the velocity state, the linearization process allows good performances thanks to the reasonably fine granularity of 1 second.

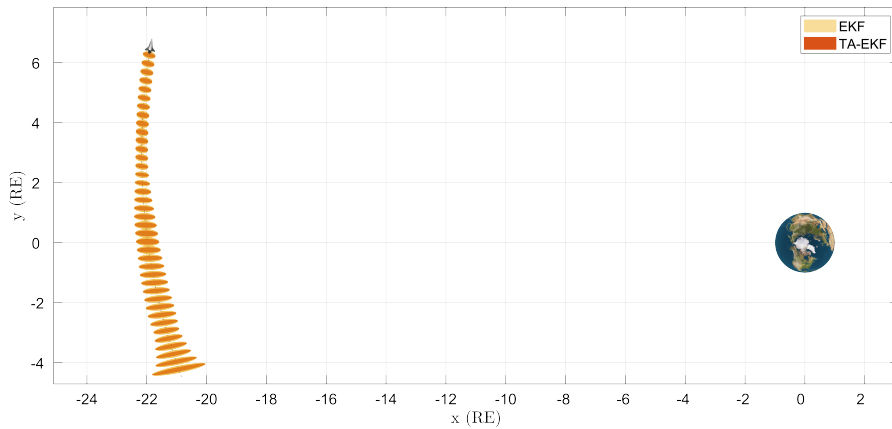


Figure 4.18: Mission point error covariance ellipsoids overview.

Finally, Figures 4.19a and 4.19b show, respectively, the positioning error time series for the plain EKF and the TA-EKF, with the 100 Monte Carlo realizations overlapped. As it was intended and as it is shown, the aided version of the Extended Kalman Filter boosts the filter convergence and reduces the positioning error.

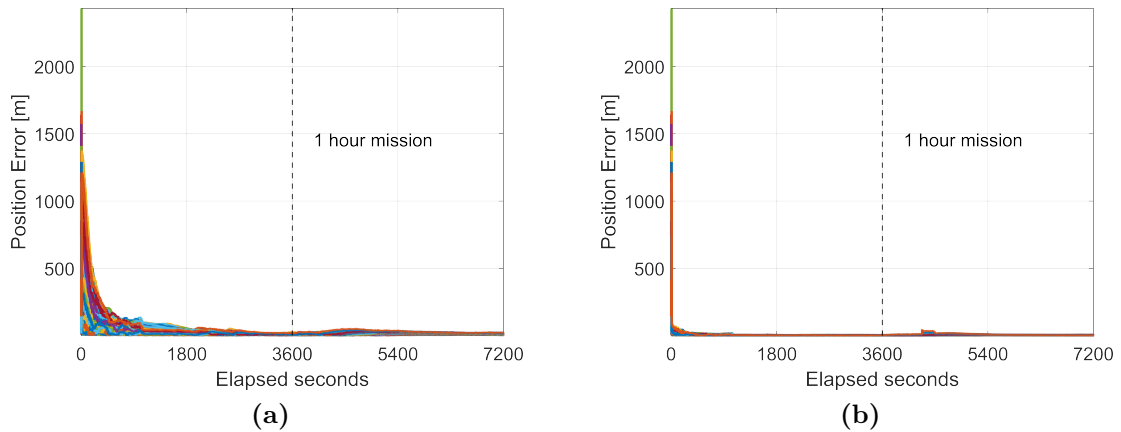


Figure 4.19: Time series of the positioning error of 100 Monte Carlo realizations. Comparison between plain EKF (a) and TA-EKF (b).

A slight hump can be observed in the position estimate error curves around epoch 4500 which might be ascribed to a lack of linearity in the spacecraft trajectory. However, further investigations ought to be carried out.

Notice that the LuGRE plan calls for mission segments that are only one hour long. Analyzing only 3600 iterations of the filters it can be seen that the convergence of the error covariance matrix is still in a transitory phase (Fig. 4.17) and, for

this particular case, the convergence is hampered by a worsening in the geometry of the problem, as highlighted by Figure 4.20. It depicts the convergence of the square root of diagonal terms of the (a-posteriori) covariance matrix P , namely the standard deviations associated with the state estimation uncertainty, for the TA-EKF. Moreover, critical points in terms of model linearization are avoided (Fig. 4.11). Anyway, the performances in terms of error in the position estimation are expected to be almost identical.

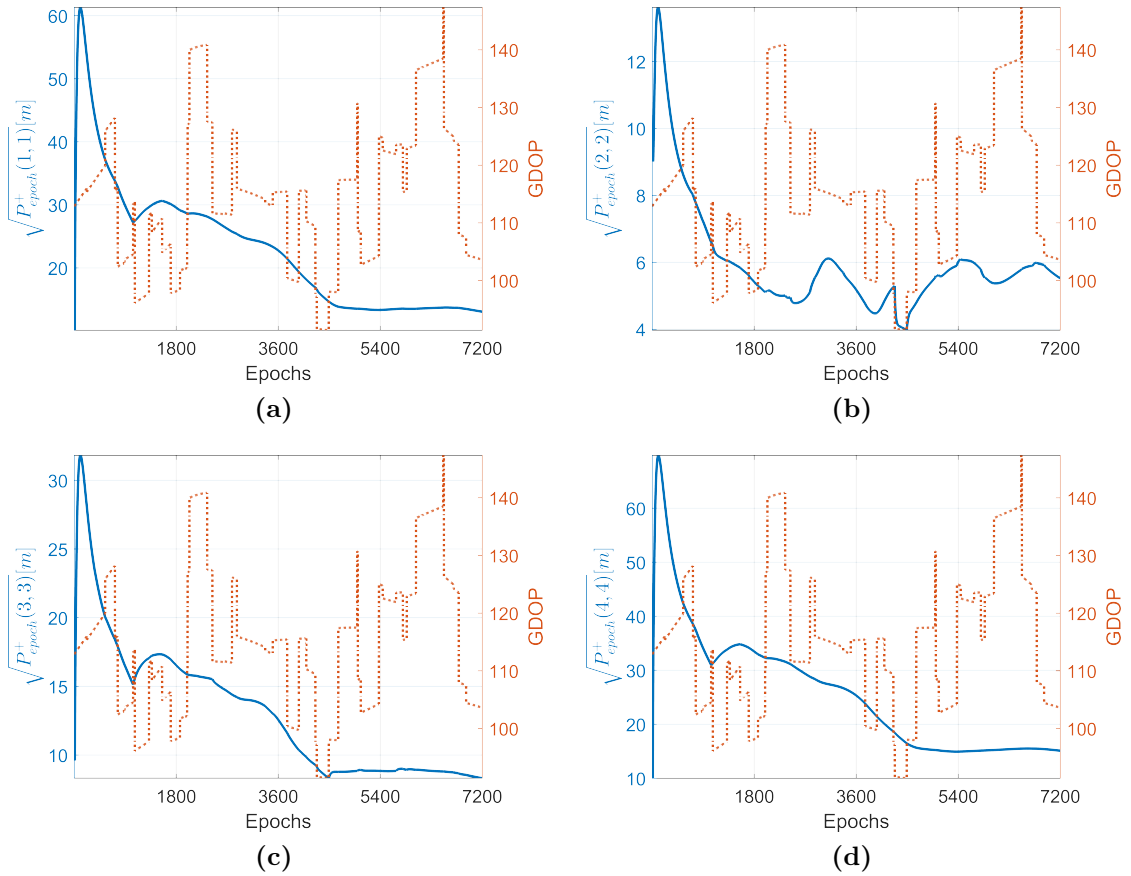


Figure 4.20: Convergence of standard deviation of state estimation uncertainty from KF compared to GDOP.

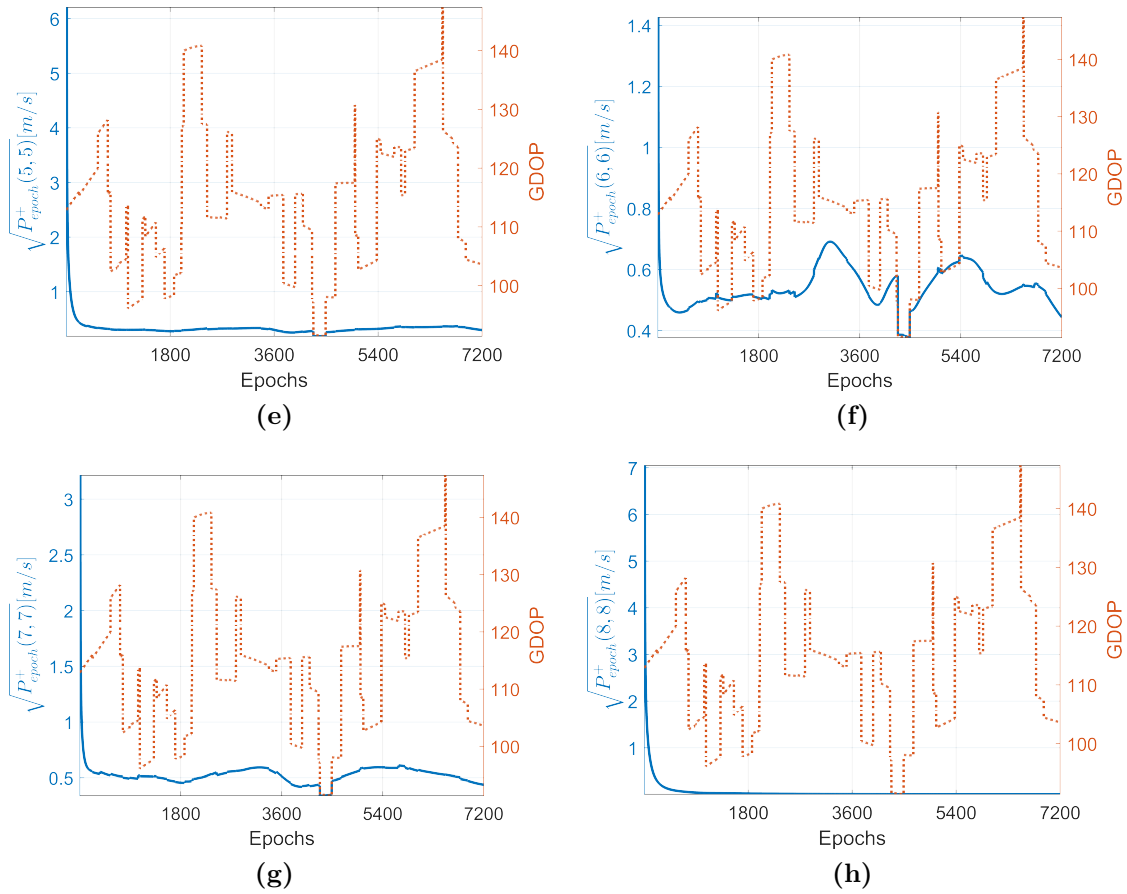


Figure 4.20: Convergence of standard deviation of state estimation uncertainty from KF compared to GDOP.

Chapter 5

Conclusions

The new space era is expected to revolutionize our approaches to space exploration, space communications, Earth observation, and many other space-related applications. However, current systems for navigation, guidance, and control of space missions typically require a reliable interaction of space and ground segments that subtends a non-negligible effort and poor spacecraft autonomy.

In the early phases of such a new era, dedicated space navigation systems are going to be designed and tested (e.g. LunaNet) while transient technologies shall support the missions. GNSS, originally designed to provide accurate Positioning, Navigation, and Timing (PNT) information to terrestrial users, is expected to be exploited for autonomous space navigation by leveraging the same multi-lateration principle that allows terrestrial users to estimate their Position, Velocity and Timing (PVT).

Indeed, Global Navigation Satellite System (GNSS) receivers in space, already validated in Low Earth Orbit (LEO), are now becoming attractive even for spacecraft navigation at larger distances, for example, in lunar missions. Exploiting GNSS as a navigation system for spacecraft approaching the Moon would ease several mission tasks. Relying on in-orbit GNSS-based navigation systems would make the spacecraft more autonomous and would reduce the costs and the efforts of federated networks, such as NASA's Deep Space Network (DSN) and the European Space Tracking Estrack network, providing tracking services. Additionally, it would pave the way to a planned space station in lunar orbit and future colonization of the Moon and then of Mars.

Nevertheless, these altitudes represent a challenging environment, characterized by high Doppler frequency and very weak signals reception, compromising the performance of actual GNSS receivers, which were not designed for non-terrestrial navigation.

This thesis introduces a customized filter, the Trajectory-Aware Extended Kalman Filter (TA-EKF), tailored to GNSS navigation throughout Earth-Moon

Transfer Orbits (MTOs). The proposed methodology demonstrates that the integration of aiding information, such as the expected orbital trajectory, can improve filter convergence and lead to highly accurate positioning solutions. This technology is especially important for non-terrestrial applications where GNSS signal availability can be significantly impaired at high altitudes, preventing the necessary accuracy for orbit determination algorithms. Through a dedicated framework simulating MTO mission scenarios and associated GNSS measurements, the performance of the proposed methodology was investigated using Monte Carlo analyses, which statistically assessed TA-EKF effectiveness against a standalone Extended Kalman Filter (EKF) architecture. Ultimately, the TA-EKF represents a significant advancement in the filtering-based estimation of PVT and serves as a valuable tool for achieving cis-lunar and lunar volume exploration using space-borne GNSS receivers. Using a dedicated simulation framework, the current study showcases the application of the TA-EKF to mitigate the negative impact of poor GNSS visibility conditions across MTOs. The TA-EKF leverages the trajectory data of a sample MTO to enhance the EKF prediction stage, resulting in approximately 88% improvement in position estimate accuracy at the 95th percentile, under favorable conditions. Additionally, the TA-EKF displays faster convergence than its unaided counterpart in both position and velocity states. Future research endeavors will quantify the effects on state estimation accuracy when inaccurate trajectory aidings are applied to the TA-EKF.

Bibliography

- [1] Joel J. K. Parker et al. *The Lunar GNSS Receiver Experiment (LuGRE)* - *NASA Technical Reports Server (NTRS)*. Feb. 2022. URL: <https://ntrs.nasa.gov/citations/20220002074> (cit. on pp. 1, 39, 40, 49, 52, 53, 61).
- [2] Robert Grover Brown and Patrick Y C Hwang. *Introduction to random signals and applied Kalman filtering with Matlab exercises*. en. 4th ed. Chichester, England: John Wiley & Sons, Jan. 2012 (cit. on pp. 15, 27, 40, 42).
- [3] Elliott D. Kaplan. *Understanding GPS: Principles and applications*. Artech House, 2006 (cit. on p. 18).
- [4] Luke B. Winternitz, William A. Bamford, Anne C. Long, and Munther Hassouneh. *GPS based autonomous navigation study for the Lunar Gateway* - *NASA Technical Reports Server (NTRS)*. Jan. 2019. URL: <https://ntrs.nasa.gov/citations/20190002311> (cit. on p. 40).
- [5] O. Montenbruck, R. Schmid, F. Mercier, P. Steigenberger, C. Noll, R. Fatkulin, S. Kogure, and A.S. Ganeshan. «GNSS satellite geometry and attitude models». In: *Advances in Space Research* 56.6 (2015), pp. 1015–1029. ISSN: 0273-1177. DOI: <https://doi.org/10.1016/j.asr.2015.06.019>. URL: <https://www.sciencedirect.com/science/article/pii/S0273117715004378> (cit. on p. 43).
- [6] USA DoD. *GLOBAL POSITIONING SYSTEM STANDARD POSITIONING SERVICE PERFORMANCE STANDARD*. <https://www.gps.gov/technical/ps/2008-SPS-performance-standard.pdf>. Sept. 2008 (cit. on p. 44).
- [7] Endrit Shehaj, Vincenzo Capuano, Cyril Botteron, Paul Blunt, and Pierre-André Farine. «GPS based navigation performance analysis within and beyond the space service volume for different transmitters' antenna patterns». In: *Aerospace* 4.3 (2017), p. 44. DOI: [10.3390/aerospace4030044](https://doi.org/10.3390/aerospace4030044) (cit. on p. 44).
- [8] W. Marquis. *The GPS Block IIR/IIR-M - Antenna Panel Pattern*. 2014. URL: https://www.navcen.uscg.gov/sites/default/files/pdf/gps/GPS_Block_IIR_IIR_M_Antenna_Panel_Pattern_Marquis_Aug2015_revised.pdf (cit. on p. 44).

-
- [9] MathWorks. *Modeling Satellite Constellations Using Ephemeris Data*. <https://it.mathworks.com/help/satcom/ug/modeling-constellation-using-ephemeris-data.html>. 2022 (cit. on p. 46).
- [10] Werner Enderle, Francesco Gini, Erik Schönemann, and Volker Mayer. *PROBA-3 precise orbit determination based on GNSS Observations*. Sept. 2019. URL: <https://www.ion.org/publications/abstract.cfm?articleID=17083> (cit. on p. 47).
- [11] «White Paper Digital Transmission : Carrier-to-Noise Ratio , Signal-to-Noise Ratio , and Modulation Error Ratio». In: 2012 (cit. on p. 49).
- [12] Heidi Kuusniemi. «User-Level Reliability and Quality Monitoring in Satellite-Based Personal Navigation». In: (Jan. 2005) (cit. on p. 55).
- [13] R.R. Bate, D.D. Mueller, and J.E. White. *Fundamentals of Astrodynamics*. Dover Books on Aeronautical Engineering Series. Dover Publications, 1971. ISBN: 9780486600611. URL: <https://books.google.it/books?id=UtJK8cetqGkC> (cit. on p. 57).
- [14] H. Curtis. *Orbital Mechanics: For Engineering Students*. Aerospace Engineering. Elsevier Science, 2015. ISBN: 9780080470542. URL: <https://books.google.it/books?id=6a09aGNBAGIC> (cit. on p. 57).
- [15] E. M. Goodger. *Principles of spaceflight propulsion*. Pergamon Press, 1970 (cit. on p. 57).
- [16] Jiangtao Fan and Guanyi Ma. «Characteristics of GPS positioning error with non-uniform pseudorange error». In: *GPS Solutions* 18.4 (2014), pp. 615–623. DOI: 10.1007/s10291-013-0359-z (cit. on p. 62).
- [17] Lauren Konitzer, Nathan Esantsi, and Joel Parker. *Navigation Performance Trades and analysis for the lunar GNSS receiver experiment (LuGRE) - NASA Technical Reports Server (NTRS)*. Aug. 2022. URL: <https://ntrs.nasa.gov/citations/20220010107> (cit. on p. 64).
- [18] Mauricio A. Caceres Duran, Pau Closas, Emanuela Falletti, Carles Fernández-Prades, Montse Nájjar, and Francesco Sottile. «Chapter 6 - Signal Processing for Hybridization». In: *Satellite and Terrestrial Radio Positioning Techniques*. Ed. by Davide Dardari, Emanuela Falletti, and Marco Luise. Oxford: Academic Press, 2012, pp. 317–382. ISBN: 978-0-12-382084-6. DOI: <https://doi.org/10.1016/B978-0-12-382084-6.00006-4>. URL: <https://www.sciencedirect.com/science/article/pii/B9780123820846000064>.

- [19] Anaïs Delépaut, Pietro Giordano, Javier Ventura-Traveset, Daniel Blonski, Miriam Schönfeldt, Philippe Schoonejans, Sarmad Aziz, and Roger Walker. «Use of GNSS for lunar missions and plans for lunar in-orbit development». In: *Advances in Space Research* 66.12 (2020). Scientific and Fundamental Aspects of GNSS - Part 1, pp. 2739–2756. ISSN: 0273-1177. DOI: <https://doi.org/10.1016/j.asr.2020.05.018>. URL: <https://www.sciencedirect.com/science/article/pii/S0273117720303410>.
- [20] Rob Rutkowski. *What's The Differences Between the 5 GNSS Constellations?* <https://blog.bliley.com/the-differences-between-the-5-gnss-satellite-network-constellations>. Jan. 2022.
- [21] EUSPA. *What is GNSS?* <https://www.euspa.europa.eu/european-space/eu-space-programme/what-gnss>. Dec. 2021.
- [22] GISGeography. *How GPS Receivers Work – Trilateration vs Triangulation*. <https://gisgeography.com/trilateration-triangulation-gps/>. May 2022.
- [23] Alex Minetto, Fabio Dovis, Andrea Nardin, Oliviero Vouch, Gabriele Impresario, and Mario Musmeci. «Analysis of GNSS data at the Moon for the LuGRE project». In: *2022 IEEE 9th International Workshop on Metrology for AeroSpace (MetroAeroSpace)*. 2022, pp. 134–139. DOI: 10.1109/MetroAeroSpace54187.2022.9855945.
- [24] Samuele Fantinato et al. «Development challenges of a GNSS SDR receiver for Moon Landing». In: *ION GNSS+, The International Technical Meeting of the Satellite Division of The Institute of Navigation* (2022). DOI: 10.33012/2022.18369.
- [25] Andrea Nardin, Alex Minetto, Oliviero Vouch, Margherita Mariani, and Fabio Dovis. «Snapshot acquisition of GNSS signals in space: A case study at lunar distances». In: *ION GNSS+, The International Technical Meeting of the Satellite Division of The Institute of Navigation* (2022). DOI: 10.33012/2022.18477.
- [26] Anaïs Delépaut, Alex Minetto, Fabio Dovis, Floor Melman, Pietro Giordano, and Javier Ventura-Traveset. «Enhanced GNSS-based positioning in space exploiting inter-spacecraft cooperation». In: *The International Technical Meeting of the The Institute of Navigation* (2022). DOI: 10.33012/2022.18214.